universität wien

MASTERARBEIT / MASTER'S THESIS

Titel der Masterarbeit / Title of the Master's Thesis

„Telechelic Star Polymers under Shear Flow“

verfasst von / submitted by

Maud Formanek BSc BSc

angestrebter akademischer Grad / in partial fulfilment of the requirements for the degree of

Master of Science (MSc)

Wien, 2016 / Vienna, 2016

Studienkennzahl lt. Studienblatt / degree programme code as it appears on the student record sheet:	A 066 876
Studienrichtung lt. Studienblatt / degree programme as it appears on the student record sheet:	Masterstudium Physik
Betreut von / Supervisor:	Univ.-Prof. Dipl.-Ing. Dr. Christos Likos
Mitbetreut von / Co-Supervisor:	

Contents

Chapter 1

Introduction and Motivation

1.1 Soft Matter and Complex Fluids

The field of *Soft Matter* concerns itself with a variety of physical, chemical and biological systems that share two important features. First of all, they are comprised of entities much larger than the typical size of atoms or simple molecules. Secondly, the energy needed to deform or alter the structure of their constituents is usually on the order of the thermal energy k_BT at room temperature. These two aspects account for the fact that many soft matter systems exhibit self-assembly behaviour, which means that the final structure and properties of a material are governed by ordered but reversibly formed aggregates of finite size interacting with each other. Due to the reversibility and the constant competition between entropic and enthalpic driving forces, it is hard – if not impossible – to infer the structure and behaviour of soft matter systems from the interaction of their smallest building blocks. However, this *softness* also makes them very interesting in terms of technological applications. In daily life, soft matter systems can be encountered as chemical products such as paints, foams, detergents, rubber, adhesives, as well as various biological materials such as milk or blood. Some prominent examples of soft matter research include

colloidal suspensions made up of spherical or rod-like solid particles of sizes between 1nm and 1μm in solution,

polymeric systems consisting of long macromolecular chains of repeated units usually covalently linked by a carbone backbone,

amphiphilic systems of molecules with both a hydrophilic – i.e. "water loving" – and a hydrophobic – i.e. "water hating" part,

active matter which has the ability to propel itself or exert mechanical forces by consuming energy.

1.2 Between Patchy Colloids and Ultrasoft Polymers: Telechelic Star Polymers

Advances in technology would not be possible without the discovery and synthesis of novel materials with a unique combination of physical and chemical properties. The enormous progress of soft matter research during the last decades brought with it the desire to create materials especially tailored to specific technological applications. Ideally, these materials would consist of highly tunable building blocks with the ability to self-assemble into a predictable shape and respond to a variety of chemical and physical stimuli. Over the past years, many studies have been conducted on complex colloids and polymers such as star-branched polyelectrolytes [1], hard colloids with functionalised attractive patches [2, 3, 4], DNA-coated colloids [5, 6], amphiphilic dendrimers [7], and microgels [8].

Recently, *telechelic star polymers* (*TSP*s), sometimes also referred to as *diblock copolymer stars* or *amphiphilic star polymers*, have proved to be a very versatile novel class of tunable molecules. They result when a number of f diblock copolymer arms are anchored to a central point. Each arm consists of a block of solvophilic monomers on the internal end and a block of solvophobic monomers on the protruding end. The term *telechelic* is derived from the two Greek words *tele* ($\tau\eta\lambda\epsilon'$), meaning "remote" or end, and *chele* ($\chi\epsilon\iota'\lambda o\varsigma$), which means "lip" or "claw" and refers to a functionalised (attractive) group in this context.

It has been shown that single *TSP*s take on various distinct conformations completely controlled by their functionality f, their fraction of solvophobic monomers per arm or amphiphilicity α and temperature [9, 10]. They self-assemble into structures with one or multiple aggregation sites or clusters of their solvophobic parts. Due to the steric repulsion of the solvophilic monomers, the arms collapsing on their ends take on a nearly ellipsoidal, bloated shape sometimes called a "watermelon" structure. When there are several aggregation sites present, these are distributed equally over the whole dihedral angle due to entropic effects and thus resemble soft penetrable colloids with attractive patches.

If the solvophobic part is longer than the solvophopilic part, i.e. $\alpha \geq 0.5$, these conformations are not stable at finite densities and the system undergoes macrophase-separation between a gas and a liquid independent of functionality [11, 12]. In the opposite case ($\alpha \leq 0.5$), however, the single star properties such as patch size, number and distribution persist even up to high concentrations [13]. Depending on the number of association sites, these systems can form spherical [11, 12] or wormlike [14] micelles for low functionality stars with only one patch or percolating networks or gels for stars with higher functionality and multiple watermelon structures [15]. Furthermore, stars that keep their single star conformation in the semidilute regime were also shown to be able to mechanically stabilize crystal

lattices which are compatible with the number of their association sites, as for example a diamond and a simple cubic lattice in the case of a four-patch star [13, 16].

1.3 Hydrodynamics and Rheology

Since non-equilibrium situations, especially flow, play a role in many technological applications and biological systems such as in microfluidics or blood flow, understanding the behaviour of patchy colloids in such environments is essential. For example, star polymers are used today in drug delivery systems [17] or as motor oil viscosity modifiers [18].

Shear flow represents the special case of a non-equilibrium stationary state, which makes it an ideal system for studying the dynamical behaviour of colloids and polymers. In dilute solutions, we might observe density fluctuations on a supramolecular level and we can measure the viscoelastic response to applied stresses. For polymers, the rheological properties can be governed by two counteracting processes: With their many fluctuating degrees of freedom, polymer gels can adapt to the flow profile, resulting in a decreasing viscosity with shear rate and so-called *shear thinning*, or polymers can be entangled with knots and loops, leading to an increase in viscosity or *shear thickening*.

Before investigating percolating networks of stars however, it is instructive to first understand the response of single star under shear flows in order to better predict possible implications on dilute solutions. Purely repulsive stars without hydrophobic end groups have already been studied in shear flow and it has been shown that their structural flexibility leads to a mutual influence of fluid and polymer, resulting in both a change in the conformation of the star and a deviation from the linear profile of the fluid [19]. Furthermore, stars with small functionality f exhibit a tumbling motion characterized by alternating collapsed and stretched conformations [19], resembling the behaviour of linear polymers [20], while high-functionality stars perform a continuous tank-treading rotation similar to fluid droplets and capsules [21].

1.4 Scope and Organisation of this Thesis

In this thesis, the behaviour of telechelic star polymers at infinite dilution under the influence of shear flow will be investigated with a special emphasis on the possible change of their patchiness and association sites.

In Chapter 2 the model of star polymers used in this work will be presented and a short review of their characteristics under equilibrium situations will be given.

Chapter 3 will give a short introduction on the governing equations of hydrodynamics

and a discussion of feasible simplifications for special systems.

Afterwards, we will transition from the theoretical description of hydrodynamics to the computational implementation thereof in Chapter 4. We will introduce in detail the mesoscopic simulation approach of *Multi-particle Collision Dynamics* and test the algorithm against theoretical predictions.

In Chapter 5, molecular dynamics and Multi-particle Collision dynamics will be combined for a hybrid simulation of telechelic star polymers under shear flow, which will represent the main body of work of this thesis.

Finally, the results will be summarized and discussed in Chapter 6 and a brief outlook on possible future extension of the topic covered in this thesis will be given.

Chapter 2

Telechelic Star Polymers

2.1 The Model

Telechelic star polymers (TSPs) are macromolecules consisting of a number of f amphiphilic arms anchored to a central point. Each of these arms is composed of a central part of N_A solvophilic monomers of type A and a tail of N_B solvophobic monomers of type B. The fraction of solvophobic monomers per arm, the amphiphilicity, is denoted by $\alpha = \frac{N_B}{N_A+N_B}$. The monomers themselves are considered to be point particles. The model of the TSP used in this thesis follows closely the work of Rovigatti, Capone and Likos [22], who studied the self-assembly scenarios of such polymers under equilibrium conditions.

Bonds between consecutive monomers are held together by a FENE (finitely extensible nonlinear elastic) potential [23] of the form

$$V_{FENE}(r) = -15\epsilon \frac{r_F^2}{\sigma^2} \log\left(1 - \frac{r^2}{r_F^2}\right) \tag{2.1}$$

where r_F is the maximum distance between linked monomers and is set to $r_F = 1.5\sigma$ for regular monomers and $r_F = 4.5\sigma$ for bonds with the central anchoring monomer — with σ being the distance at which an unshifted Lennard–Jones (LJ) potential [24] is zero. The parameter ϵ denotes the interaction strength. In the following it is assumed that $\sigma = 1$, $\epsilon = 1$, $k_B = 1$ (Boltzmann's constant) and $m = 1$ (monomer mass) and all dimensional quantities such as length, time and temperature are scaled accordingly. Additionally, all monomers of type A interact with other monomers of type A as well as with monomers of type B via a generalized repulsive Lennard–Jones (LJ) potential,

$$V_{AA}(r) = V_{AB}(r) = \begin{cases} 4\epsilon\left[\left(\frac{r}{\sigma}\right)^{48} - \left(\frac{r}{\sigma}\right)^{24}\right] + \epsilon & \text{if } r < r_{rep}^c, \\ 0 & \text{otherwise} \end{cases} \tag{2.2}$$

with a cutoff distance $r_{rep}^c = 2^{\frac{1}{24}} \approx 1.03$.

Furthermore, the interaction of the solvophobic B-monomers is governed by addition of an attractive tail to the former generalized LJ potential 2.3, rescaled by a factor λ, which serves as an inverse temperature:

$$V_{BB}(r) = \begin{cases} V_{AA}(r) - \lambda & \text{if } r < r_{rep}^{c}, \\ 4\lambda \left[\left(\frac{r}{\sigma}\right)^{48} - \left(\frac{r}{\sigma}\right)^{24} \right] & \text{otherwise} \end{cases} \tag{2.3}$$

To improve performance, this potential is truncated at $r_c = 1.5$. Since this truncation creates a discontinuity in the potential which would violate energy conservation when two particles cross this boundary [25], the potential is also shifted such that $V_{BB}(r_c) = 0$.

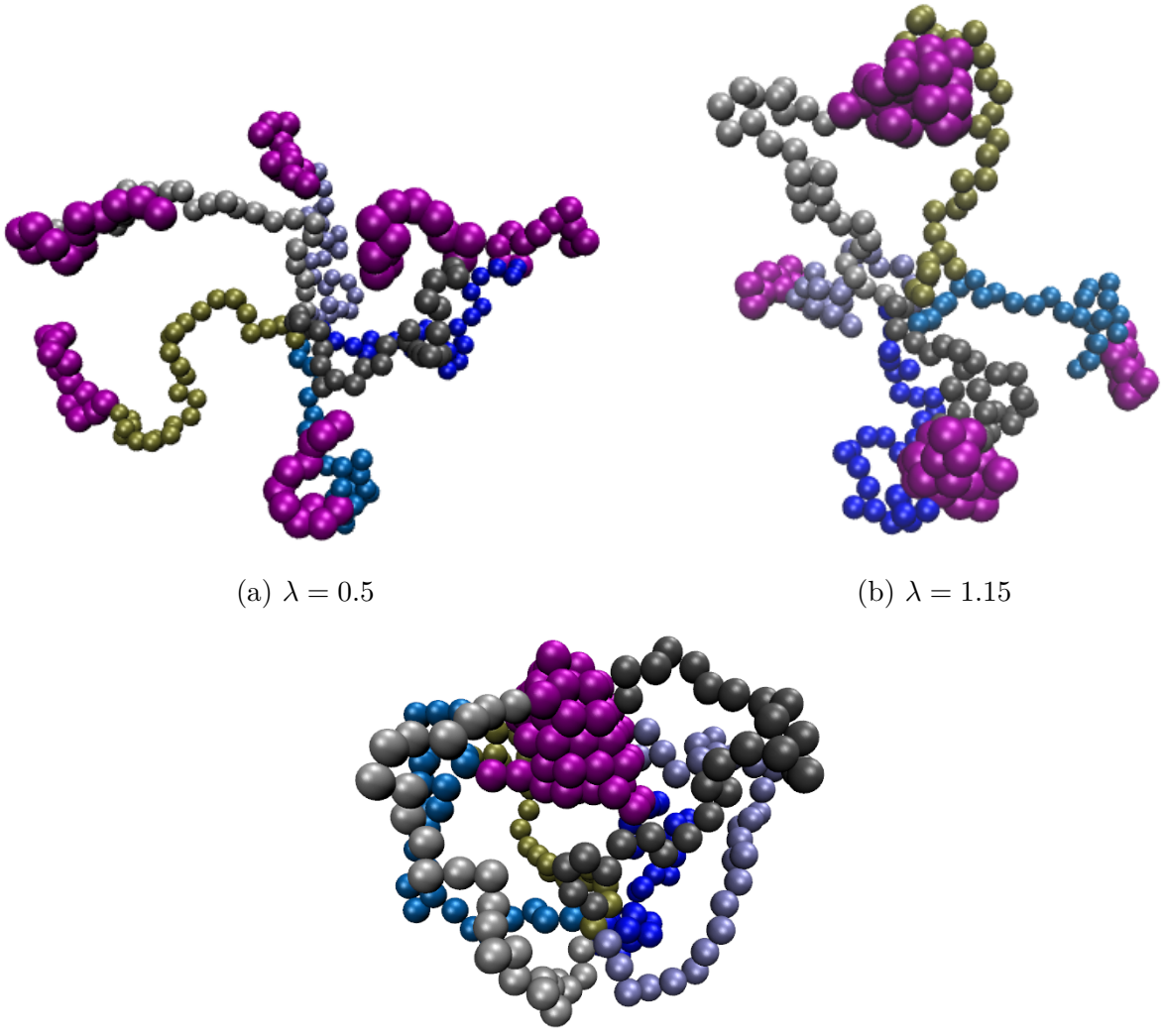

(a) $\lambda = 0.5$

(b) $\lambda = 1.15$

(c) $\lambda = 1.35$

Figure 2.1: Representative conformations of a TSP with $f = 6$ with different interaction strengths λ. Purple spheres correspond to solvophobic B-type monomers. Solvophilic A-type monomers are coloured in different shades of grey and blue according to which arm they belong to.

Figure 2.1 shows snapshots of typical conformation of a TSP with $f = 6$ and $\alpha = 0.3$ at different values of the attraction coupling constant λ. The image illustrates the self-assembly process taking place with increasing λ. At small values of λ, both A and B type monomers are in good solvent conditions and the TSP takes on an open configuration resembling that of athermal stars [26]. When the value of λ is increased, however, the interaction between B monomers becomes stronger, i.e. the solvent quality is worsened for B monomers, and they form patches among themselves, connecting different arms. For very high values of λ, all arms collapse onto one patch, given that the number of monomers per arm L_f is big enough to compensate the steric repulsion of the A-type monomers. The ellipsoidal shape of a star with many arms collapsing onto one patch is sometimes called a *watermelon* structure.

2.2 Results in Equilibrium

In the following section, we will give a brief introduction on the characteristics investigated in this thesis, and we will present results of preliminary equilibrium simulations of telechelic star polymers. These results were obtained using molecular dynamics simulations (*cf.* 5.1) with implicit solvent – i.e. no hydrodynamic interactions are taken into account –, with a time-step of $\Delta t = 0.001$ and a temperature of $k_B T = 0.5$. Functionalities f of 6, 9 and 15 as well as values of α of 0.3 and 0.5 are considered. The degree of polymerization L_f – i.e. the number of monomers per arm – is 40 for all stars regardless of functionality. The attraction coupling constant λ ranges from 0.8 to 1.4.

2.2.1 Characterisation of Patchiness

In order to characterize the telechelic stars we first analyse the patches into which their arms self-assemble. Patches are defined by a clustering algorithm, where two arms are said to belong to the same cluster if at least two of their B-monomers experience a net attraction between them – i.e. their pair-wise energy is less than zero. From this, we calculate the average number of patches N_p and the average size of the patches s_p – where only patches of size ≥ 2 are considered. In the good solvent limit ($\lambda \to 0$), as well as for amphiphilicities $\alpha < 0.3$ [13, 16], no patches are formed in equilibrium situations (for the values of λ taken into account in this work) since the entropic intra-star repulsions dominate over the enthalpic attractions between the solvophobic tails and the stars behave in the same manner as athermal stars [26].

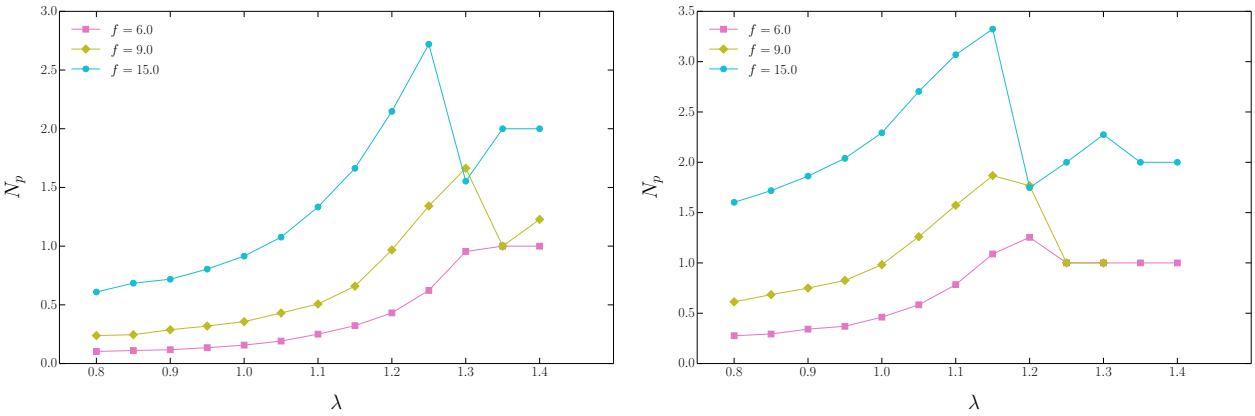

(a) $\alpha = 0.3$ (b) $\alpha = 0.5$

Figure 2.2: Number of patches N_p as a function of λ for different functionalities f and amphiphilicities α

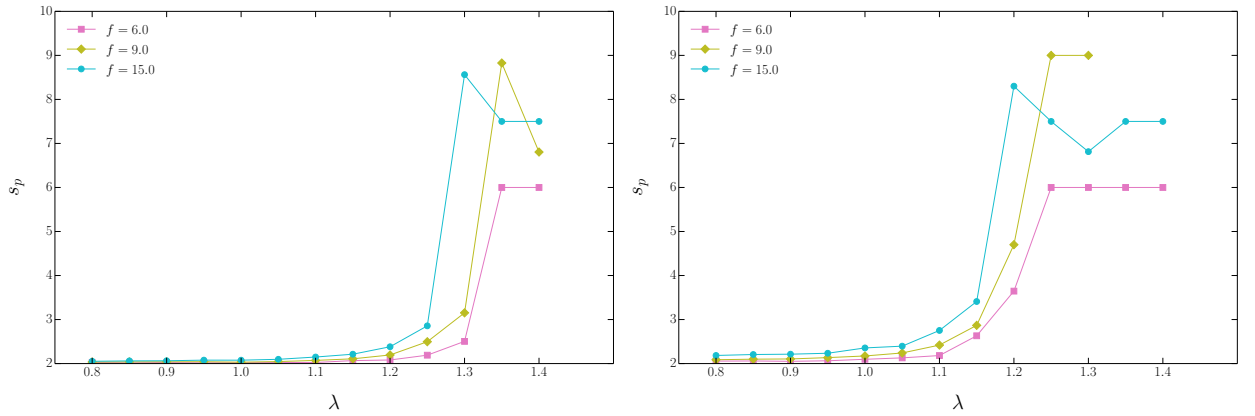

(a) $\alpha = 0.3$ (b) $\alpha = 0.5$

Figure 2.3: Patch-size s_p as a function of λ for different functionalities f and amphiphilicities α

Figure 2.2 and 2.3 show the average number of patches N_p and the average size of patches s_p formed, respectively, for the equilibrium situation without shear or hydrodynamic interactions.

For small values of λ, patch number N_p and patch size s_p increase monotonically with λ for all combinations of f and α considered. However, this monotonic behaviour is only continued to high values of α for stars of low functionality and amphiphiphilicity, e.g. $f = 6$ and $\alpha = 0.3$. This specific star architecture reaches a plateau at $\lambda = 1.3$, where all arms are collapsed onto one patch. The curves of all other star architectures considered exhibit a clear non-monotonicity for high values of α. For more than six arms, it is more favourable for the stars to form more than one patch due to the steric repulsion between A-type monomers

and the entropic cost of the completely collapsed conformation. Above a certain threshold, however, the enthalpic contribution of the B-type monomers dominates and different patches start feeling a strong mutual attraction, which leads to the formation of fewer patches of greater size.

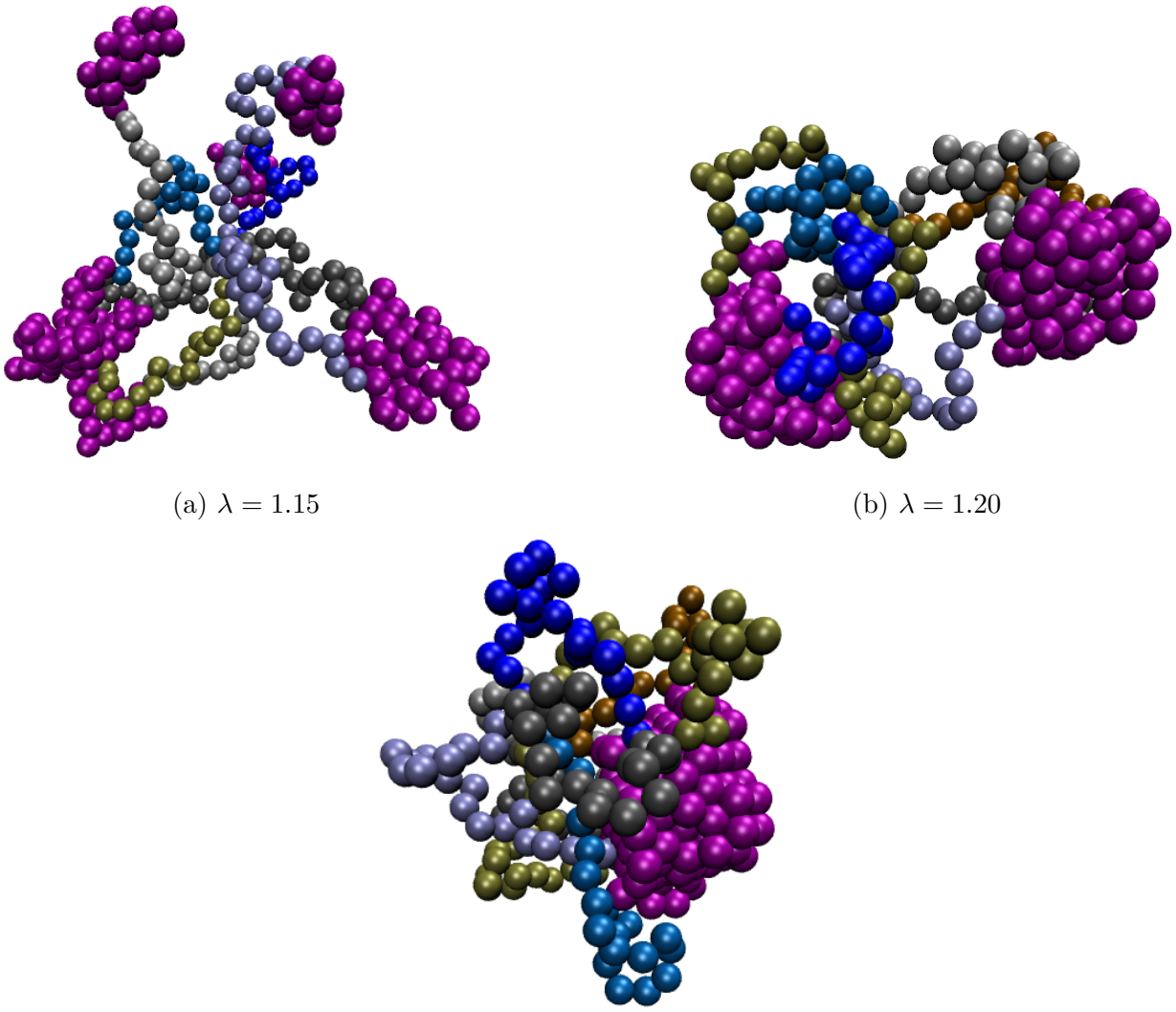

(a) $\lambda = 1.15$ (b) $\lambda = 1.20$

(c) $\lambda = 1.25$

Figure 2.4: Representative conformations of a TSP with $f = 9$ with different interaction strengths λ. Purple spheres correspond to solvophobic B-type monomers. Solvophilic A-type monomers are coloured in different shades of grey and blue according to which arm they belong to.

The snapshots of typical conformations of a star with 9 arms and an amphiphilicity of $\alpha = 0.3$, as shown in figure 2.4, visualize this behaviour. At $\lambda = 1.15$, the star polymer forms on average two highly dynamical patches and free arms still exists. Slightly lowering the temperature, i.e. $\lambda = 1.20$, leads to the collapse of the remaining free arms onto the

already formed patches. Finally, at $\lambda \geq 1.25$, the attraction between B-monomers is high enough to overcome the entropic cost of merging two patches into one. The same is true for TSPs with 15 arms, the only difference being that the favoured number of patches changes from three to two. A comparison between the behaviour of stars of different amphiphilicity α suggests that the onset of the non-monotonic dependence of patch size and patch number on λ occurs at at lower values of λ for higher values of α.

2.2.2 Conformation and Shape Parameters

In order to investigate the shape of the TSPs, we follow the method of using the principal moments of the gyration tensor to analyse polymer conformations first proposed by Šolc and Stockmayer in 1973 [27]. To this end, we define the *radius of gyration tensor* of a configuration of a polymer as

$$G_{\alpha\beta} \coloneqq \frac{1}{N}\sum_{i=1}^{N}\left(r_{i,\alpha} - r_{cm,\alpha}\right)\left(r_{i,\beta} - r_{cm,\beta}\right) \tag{2.4}$$

$$= \frac{1}{N^2}\sum_{j>i}^{N}(r_{i,\alpha} - r_{j,\alpha})(r_{i,\beta} - r_{j,\beta})\,, \tag{2.5}$$

where N is the total number of monomers of a star, $r_{i,\alpha}$ is the α-th Cartesian component of monomer i in the polymer (where $\alpha, \beta = \{x, y, z\}$) and r_{cm} is the position of the polymer's center-of-mass. Both definitions presented are equivalent, however, we will use the first one in the following discussion. The shape of polymers can be conveniently analysed by changing to the principal axis system of G – i.e. the system in which G is diagonal –

$$G = \mathrm{diag}(\lambda_1, \lambda_2, \lambda_3)\,, \tag{2.6}$$

with eigenvalues λ_i in descending order ($\lambda_1 \geq \lambda_2 \geq \lambda_3$). The three eigenvectors corresponding to the three eigenvectors define an ellipsoid which has the same inertial properties as the polymer. The tensor G has three invariants, namely its trace

$$I_1 \coloneqq \mathrm{tr}(G) = \lambda_1 + \lambda_2 + \lambda_3\,, \tag{2.7}$$

which corresponds to the squared *radius of gyration*, its determinant

$$I_2 \coloneqq \det(G) = \lambda_1\lambda_2\lambda_3\,, \tag{2.8}$$

and the sum of its three principal minors

$$\begin{aligned} I_3 &\coloneqq \frac{1}{2}\left((\mathrm{tr}(G))^2 - \mathrm{tr}(G^2)\right) \\ &= G_{11}G_{22} + G_{11}G_{33} + G_{22}G_{33} - G_{12}G_{21} - G_{13}G_{31} - G_{23}G_{32} \\ &= \lambda_1\lambda_2 + \lambda_1\lambda_3 + \lambda_2\lambda_3 \end{aligned} \tag{2.9}$$

These invariants can now be used along with the eigenvalues of G to define shape parameters which we will later use to describe the conformations of the TSPs. First, we introduce a measure for the polymer's deviation from a spherical shape, the *asphericity* δ [28, 29, 30, 31, 32]

$$\delta := \frac{\langle I_1^2 - 3I_3 \rangle}{\langle I_2^2 \rangle} = 1 - 3\langle \frac{I_2}{I_1^2} \rangle \,. \tag{2.10}$$

It ranges from 0 for objects with spherical symmetry to 1 for perfectly straight chains or rods.

In order to distinguish between prolate and oblate conformations, it is useful to introduce the *prolateness parameter* S [30, 33, 31]

$$S := \langle \frac{(3\lambda_1 - I_1)(3\lambda_2 - I_1)(3\lambda_3 - I_1)}{I_1^2} \rangle \,, \tag{2.11}$$

which can range from -0.25 to 2, where negative values are associated with predominantly oblate shapes while positive values correspond to moreover prolate shapes.

Finally, we define the *acylindricity* c [28, 32]

$$c := \langle \frac{\lambda_2 - \lambda_3}{I_1} \rangle \tag{2.12}$$

which is always greater or equal to zero and reaches zero only for shapes with cylindrical symmetry.

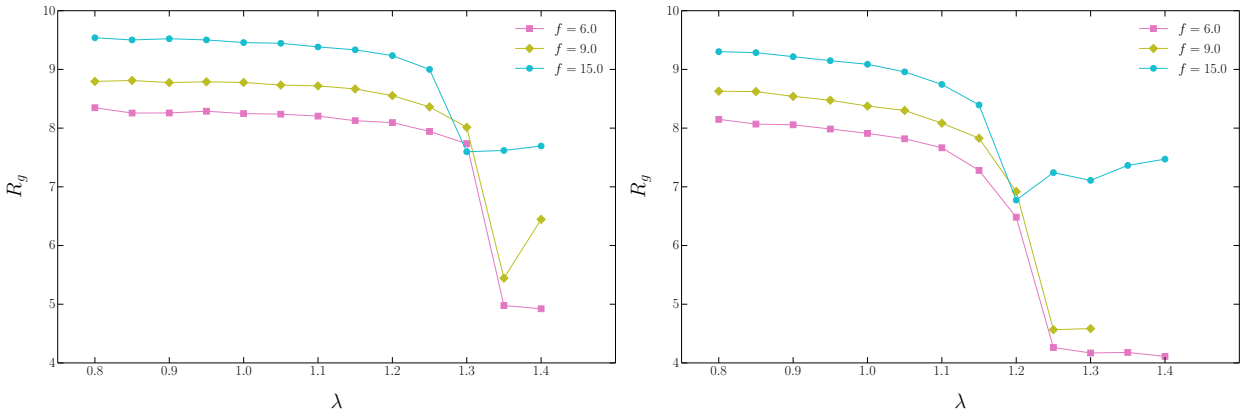

(a) $\alpha = 0.3$ (b) $\alpha = 0.5$

Figure 2.5: Radius of gyration R_g as a function of λ for different functionalities f and amphiphilicities α

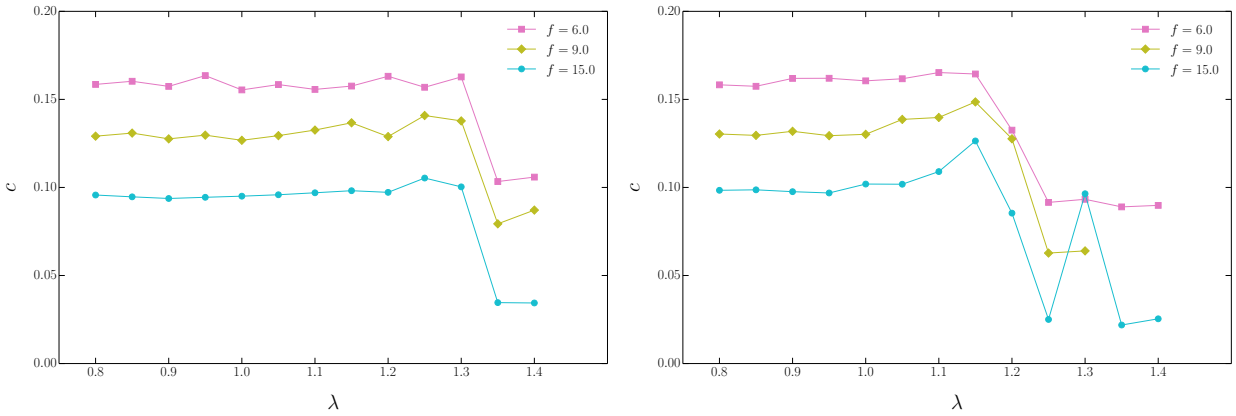

(a) $\alpha = 0.3$ (b) $\alpha = 0.5$

Figure 2.6: Acylindricity c as a function of λ for different functionalities f and amphiphilicities α

Figures 2.5, 2.8, 2.7 and 2.6 show the radius of gyration R_g, the asphericity δ, the prolateness S and the acylindricity c, respectively, for stars in equilibrium. For all stars, we see that the radius of gyration depends predominantly on the number of patches they form – with stars forming fewer patches having a smaller radius of gyration –, while their functionality is of lesser importance. Secondly, we notice that the prolateness S and the asphericity qualitatively exhibit the same behaviour. Thus, the asphericity δ will not be included in all subsequent data analysis. It is also worth noting that the prolateness S is always positive throughout the whole parameter space considered, indicating that the stars always take on a prolate shape, which has also been shown for chain- and ring polymers [34]. Like the radius of gyration, the prolateness exhibits a strong correlation with the number of patches formed. For stars which form only one patch, e.g. $f = 6$ and $\alpha = 0.3$, S reaches almost zero, which is representative of a spherical conformation. Extremely prolate shapes, on the other hand, are always associated with two patches.

Furthermore, all shape parameters are roughly constant with increasing λ, up to a certain threshold value which coincides with the value at which the size of the patches starts deviating from 2. This indicates that the onset of patch formation begins with several pairs of arms getting close to each other without affecting the shape. Upon further increasing the attraction between B-monomers, these patch-precursors align to form patches whose size and number is governed by the star-architecture.

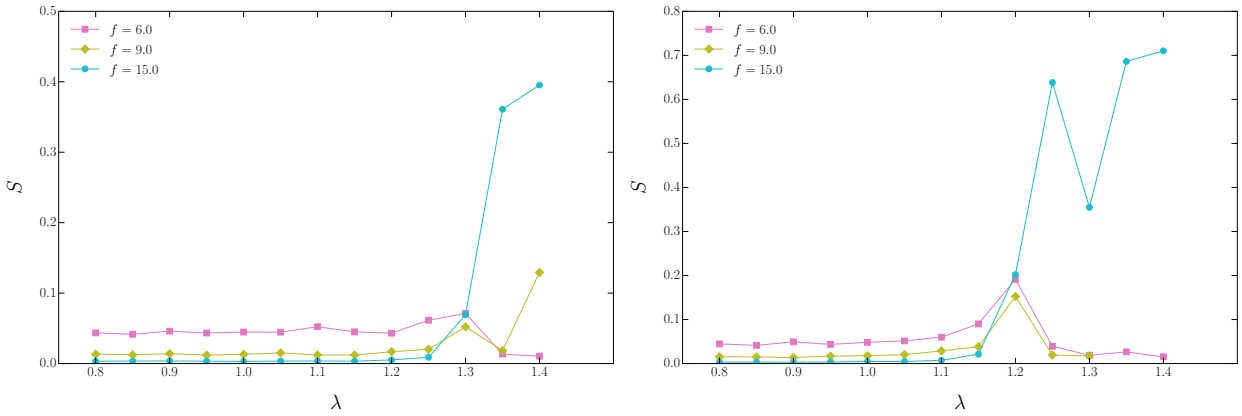

(a) $\alpha = 0.3$ (b) $\alpha = 0.5$

Figure 2.7: Prolateness parameter S as a function of λ for different functionalities f and amphiphilicities α

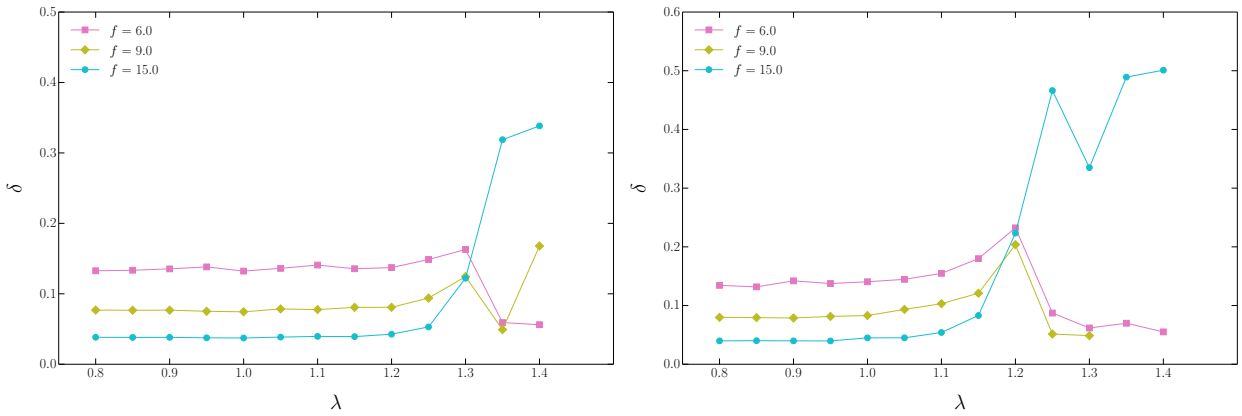

(a) $\alpha = 0.3$ (b) $\alpha = 0.5$

Figure 2.8: Asphericity δ as a function of λ for different functionalities f and amphiphilicities α

Finally, it should be noted that the behaviour of all of the characteristics presented here is shifted in λ compared to previous results presented in the work of Rovigatti *et al.* [22] – an effect than can probably be attributed to the significantly smaller number of monomers per arm L_f used here, which increases the relative contribution of the steric repulsion between the A-blocks.

2.2.3 Orientational Resistance

Once the telechelic star polymers are subjected to a fluid undergoing shear flow, it will be interesting to see how the polymer reacts to this change of environment. A good measure for the resistance of a macromolecule againt orientation in a flow field is its orientational resistance m_g [35], which is related to the angle χ_g between the flow direction x and the eigenvector of the gyration tensor with the largest eigenvalue $\hat{\boldsymbol{e}}_1$ as depicted in figure 2.9. It is defined as

$$m_g = \mathrm{Wi} \tan 2\chi_g \,, \tag{2.13}$$

and can be calculated from the gyration tensor of the polymer according to

$$\tan 2\chi_g = \frac{2G_{xy}}{(G_{xx} - G_{yy})} \,. \tag{2.14}$$

For a detailed derivation the interested reader is referred to Appendix B.

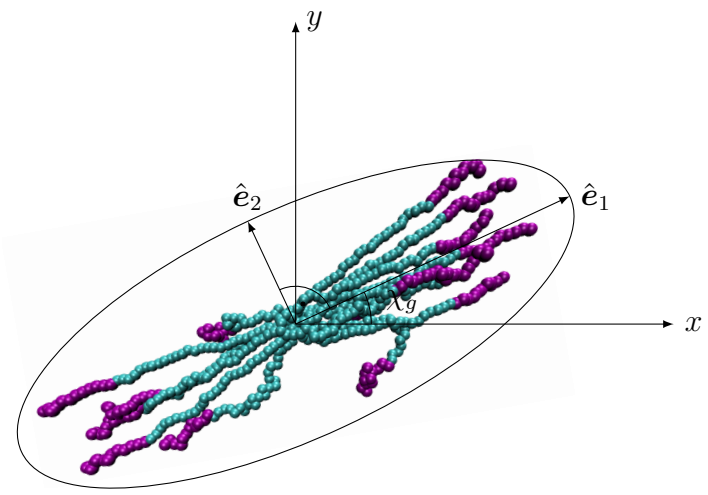

Figure 2.9: orientation angle χ_g

The dimensionless quantity Wi is called the Weissenberg number and is a function of the shear rate $\dot{\gamma}$ and the longest relaxation time τ of the polymer in equilibrium

$$\mathrm{Wi} = \dot{\gamma}\tau \,. \tag{2.15}$$

Within the theory of Zimm dynamics the blob model of star polymers without amphiphilic properties and a large number of arms f predicts [36]

$$\tau = \tau_0 L_f^{3\nu} f^{1-3\nu/2} \,, \tag{2.16}$$

with a Flory exponent of $\nu = 0.6$ and

$$\tau_0 = \frac{\eta b^3}{k_B T} \,, \tag{2.17}$$

where η denotes the solvent viscosity, k_BT the thermal energy and b the bond length, which we define here to be the distance between two solvophilic monomers with the minimal energy.

The reason for multiplying with the dimensionless Weissenberg number Wi for the definition of the orientational resistance m_g lies in the fact that for small shear rates $G_{xy} \sim \dot{\gamma}$ and $(G_{xx} - G_{yy}) \sim \dot{\gamma}^2$ has been found for several systems including rodlike colloids and linear polymers [37, 38, 39], which leads to a nonvanishing value for the orientational resistance m_g in the limit of zero shear rate (i.e. Wi $\longrightarrow 0$).

Chapter 3

Hydrodynamics

Hydrodynamics is the theory of motion of fluids. Since it concerns itself with their macroscopic properties, fluids are regarded as continuous media instead of as an ensemble of individual atoms. Hence, when we speak of infinitely small volume elements of such a fluid, we mean infinitely small compared to the total volume under consideration, but still large compared to the typical sizes and distances on a molecular level. In consequence, properties of any small volume element are considered to be well-defined averages over its molecular constituents. Mathematically, fluid flow is described by its velocity field $\boldsymbol{v}(\boldsymbol{r}, t)$ and any other two of its thermodynamic properties, such as pressure $p(\boldsymbol{r}, t)$ and mass density $\rho(\boldsymbol{r}, t)$. In the following, a short introduction into the mathematical description of fluids will be given. For a more detailed explanation on the fundamentals of fluid dynamics, the reader is referred to the introductory textbook *Fluid Mechanics* by Landau and Lifshitz [40] or *Statistical Mechanics of Nonequilibrium Fluids* by Evans and Morriss [41].

3.1 The Continuity Equation

Let us begin the derivation of the governing equations of fluid dynamics by considering the change of mass in a certain volume V_0. If we denote the mass density at a given point $\boldsymbol{r}$ at time t by $\rho(\boldsymbol{r}, t)$, the total mass M in the volume V_0 is given by the integral

$$M = \int_{V_0} \rho \, \mathrm{d}V \,. \tag{3.1}$$

The amount of fluid that leaves the volume V_0 per unit time is given by the flow through its boundaries

$$\oint_{\partial V_0} \rho \, \boldsymbol{v} \cdot \mathrm{d}\boldsymbol{f} \,, \tag{3.2}$$

where $\rho\boldsymbol{v}$ is called the mass flux density and $d\boldsymbol{f}$ is a vector normal to a surface element of the volume V_0, which points outward and has a magnitude equal to the area of the surface

element. This loss of mass through the boundaries has to be equal to the negative change in total mass inside the volume and thus we arrive at

$$\frac{\partial}{\partial t}\int \rho \,\mathrm{d}V = -\oint \rho \boldsymbol{v} \cdot \mathrm{d}\boldsymbol{f}\,. \tag{3.3}$$

Applying Green's formula to the surface integral on the right hand transforms it into a volume integral

$$\oint \rho \boldsymbol{v} \cdot \mathrm{d}\boldsymbol{f} = \int \boldsymbol{\nabla} \cdot (\rho \boldsymbol{v})\,\mathrm{d}V \tag{3.4}$$

Accordingly, equation 3.2 becomes

$$\int \left[\frac{\partial \rho}{\partial t} + \boldsymbol{\nabla} \cdot (\rho \boldsymbol{v})\right] \mathrm{d}V = 0\,. \tag{3.5}$$

This equation must hold for any volume and thus the integrand must vanish and we arrive at the *continuity equation*:

$$\frac{\partial \rho}{\partial t} + \nabla \cdot (\rho \boldsymbol{v}) = 0\,. \tag{3.6}$$

3.2 Ideal Fluids and Euler's Equation

In the simplest case, there is no energy dissipation due to internal friction or heat exchange. Fluids, for which these two processes can be neglected are called *ideal fluids* and we will take a look at their equations of motions in the following. First, consider some volume of the fluid. In the absence of shear forces the total force acting on it is equal to the total pressure acting normal to its surface

$$\boldsymbol{F} = -\oint p\,\mathrm{d}\boldsymbol{f} = -\int \nabla p\,\mathrm{d}V\,, \tag{3.7}$$

where the second equivalence follows from the gradient theorem. This means that the surrounding fluid exerts a force $-\nabla p$ on a unit volume. Inserting this into Newton's equation of motion for the fluid's mass density yields

$$\rho \frac{\mathrm{d}\boldsymbol{v}}{\mathrm{d}t} = -\nabla p\,. \tag{3.8}$$

It is important to note here that the derivative $\frac{\mathrm{d}\boldsymbol{v}}{\mathrm{d}t}$ refers to the change of velocity of a particular amount of the fluid as it propagates in time and space. However, since we study the fluid in terms of velocity fields which are defined for fixed points in space, we have to express this derivative differently. In order to do so, we split the substantial derivative $\frac{\mathrm{d}\boldsymbol{v}}{\mathrm{d}t}$ into two terms — one corresponding to the change in velocity per time $\mathrm{d}t$ at a fixed point in space, and one reflecting the change in velocity between two points being $\mathrm{d}\boldsymbol{r}$ apart, i.e.

$$\frac{\mathrm{d}\boldsymbol{v}}{\mathrm{d}t} = \frac{\partial \boldsymbol{v}}{\partial t} + (\boldsymbol{v} \cdot \boldsymbol{\nabla})\boldsymbol{v}\,. \tag{3.9}$$

Thus, equation 3.8 becomes

$$\frac{\partial \boldsymbol{v}}{\partial t} + (\boldsymbol{v} \cdot \boldsymbol{\nabla})\boldsymbol{v} = -\frac{1}{\rho}\nabla p\,, \tag{3.10}$$

which is known as *Euler's equation* and was first derived in 1755.

Euler's equation has another useful formulation in terms of the evolution of the fluids momentum density $\rho\boldsymbol{v}$. Applying the *continuity equation* (3.6) allows us to calculate

$$\begin{aligned}\frac{\partial}{\partial t}(\rho v_i) &= \rho\frac{\partial v_i}{\partial t} + v_i\frac{\partial \rho}{\partial t}\,,\\ &= \rho\frac{\partial v_i}{\partial t} - v_i\frac{\partial(\rho v_j)}{\partial x_j}\,.\end{aligned} \tag{3.11}$$

The term $\frac{\partial v_i}{\partial t}$ can be rewritten with the help of *Euler's equation* (3.10)

$$\frac{\partial v_i}{\partial t} = -v_j\frac{\partial v_i}{\partial x_j} - \frac{1}{\rho}\frac{\partial p}{\partial x_i} = -v_j\frac{\partial v_i}{\partial x_j} - \frac{1}{\rho}\delta_{ij}\frac{\partial p}{\partial x_j}\,. \tag{3.12}$$

Defining the momentum flux density tensor Π_{ij} as

$$\Pi_{ij} = p\delta_{ij} + \rho v_i v_j \tag{3.13}$$

we finally arrive at an equation for the evolution of the momentum flux density in terms of the momentum flux density tensor

$$\frac{\partial}{\partial t}(\rho v_i) = -\frac{\partial \Pi_{ij}}{\partial x_j}\,. \tag{3.14}$$

Physically, Π_{ij} describes the ith component of momentum flowing through a unit surface area perpendicular to the j-axis per unit time.

3.3 Energy Dissipation and the Navier Stokes Equation

In the previous sections, ideal fluids were described by completely reversible transfers of momentum due to mechanical propagation of fluid particles and pressure gradients. In real fluids, however, irreversibility is introduced into the system due to internal friction and thermal conduction. In the following, these effects of energy dissipation will be discussed and accounted for by making the necessary adaptations in *Euler's equation*.

Internal friction occurs when momentum is transferred from locations with high fluid velocity to locations where the fluid velocity is smaller. Such viscous transfer of momentum can be incorporated into the equations of motion by adding a term $-\sigma'_{ij}$ to the momentum flux density tensor (cf. equation 3.13)

$$\Pi_{ij} = p\delta_{ij} + \rho v_i v_k - \sigma'_{ij}\,. \tag{3.15}$$

Since internal friction arises from different parts of the fluid moving with different velocities and has to vanish for a constant velocity field, σ'_{ij} can only be dependent upon spacial derivatives of the fluid velocity $\partial v_i/\partial x_j$. Given that the fluid is sufficiently fine-grained such that velocity gradients are small, we can assume that σ'_{ij} contains only first derivatives of the velocity. Furthermore, σ_{ij} must vanish if the fluid is subjected to a uniform rotation around an axis ω, i.e. $\boldsymbol{v}(\boldsymbol{r},t) = \boldsymbol{\omega} \times \boldsymbol{r}$, because one can change to a co-rotating reference frame, in which the entire fluid is at rest. Hence, σ'_{ij} must be a symmetric tensor. Imposing these conditions, we can write it in the form

$$\sigma'_{ij} = a\left(\frac{\partial v_i}{\partial x_j} + \frac{\partial v_j}{\partial x_i}\right) + b\frac{\partial v_k}{\partial x_k}\delta_{ij} \tag{3.16}$$

However it will be convenient later to decompose this into a traceless and a diagonal part by introducing the *dynamic viscosity* $\eta \coloneqq a$ and the *second viscosity* $\zeta \coloneqq b + \frac{2}{3}a$ and rewriting equation 3.16 as

$$\sigma'_{ij} = \eta\left(\frac{\partial v_i}{\partial x_j} + \frac{\partial v_j}{\partial x_i} - \frac{2}{3}\delta_{ij}\frac{\partial v_k}{\partial x_k}\right) + \zeta\delta_{ij}\frac{\partial v_k}{\partial x_k}\,. \tag{3.17}$$

Inserting the modified momentum flux tensor Π_{ij} into Euler's equation (3.10) and assuming that the viscosity coefficients η and ζ are constant throughout the fluid — which doesn't hold in general, but is a good approximation in most cases —, we finally obtain

$$\rho\left(\frac{\partial \boldsymbol{v}}{\partial t} + (\boldsymbol{v}\cdot\boldsymbol{\nabla})\boldsymbol{v}\right) = -\nabla p + \eta\Delta\boldsymbol{v} + (\zeta + \frac{1}{3}\eta)\boldsymbol{\nabla}(\boldsymbol{\nabla}\cdot\boldsymbol{v})\,, \tag{3.18}$$

or, alternatively, by defining the *stress tensor* $\sigma_{ij} \coloneqq -p\delta_{ij} + \sigma'_{ij}$

$$\rho\left(\frac{\partial \boldsymbol{v}}{\partial t} + (\boldsymbol{v}\cdot\nabla)\boldsymbol{v}\right) = \nabla\cdot\boldsymbol{\sigma}\,. \tag{3.19}$$

This equation is called the *Navier–Stokes equation*. If the fluid is additionally subjected to an external force field, the force density $\boldsymbol{f}^{ext}$ would have to be added to the right side of the equation. For incompressible fluids, i.e. $\frac{\partial\rho}{\partial t} = 0$, we notice that $\boldsymbol{\nabla}\cdot\boldsymbol{v} = 0$ follows from the continuity equation (3.6) and the viscous stress tensor reduces to $\sigma_{ij} = \eta\left(\frac{\partial v_i}{\partial x_j} + \frac{\partial v_j}{\partial x_i}\right)$. Finally, we find the *Navier–Stokes equation* for incompressible fluids

$$\rho\left(\frac{\partial \boldsymbol{v}}{\partial t} + (\boldsymbol{v}\cdot\boldsymbol{\nabla})\boldsymbol{v}\right) = -\nabla p + \eta\Delta\boldsymbol{v}\,. \tag{3.20}$$

3.4 Linearized Hydrodynamics

Let us now take a look at the relative magnitudes of the terms appearing in the *Navier–Stokes equation* for incompressible fluids (3.20). In order to do so, we rescale all variables according to [42]

$$\boldsymbol{v} \to \frac{\boldsymbol{v}}{u}\,, \qquad \boldsymbol{r} \to \frac{\boldsymbol{r}}{L}\,, \qquad t \to \frac{t}{\tau}\,, \tag{3.21}$$

where u is a typical velocity – e.g. the average speed of a colloid embedded in the fluid –, L is a typical length – e.g. the diameter of such a colloid – and τ is a typical timescale – e.g. the average time between consecutive collisions of colloids. Rewriting equation 3.20 in terms of these new variables and multiplying by $L^2/(\eta u)$ yields

$$\frac{\rho L^2}{\eta\tau}\frac{\partial \boldsymbol{v}}{\partial t} + \frac{\rho u L}{\eta}(\boldsymbol{v}\cdot\boldsymbol{\nabla})\boldsymbol{v} = -\boldsymbol{\nabla}p + \Delta\boldsymbol{v}\,, \tag{3.22}$$

where the pressure p is also a dimensionless quantity after rescaling. The dimensionless quantity

$$\mathrm{Re} := \frac{\rho u L}{\eta} \tag{3.23}$$

is known as the *Reynolds number* [43, 44] and is a measure for the relative magnitude of inertial to viscous forces. Its value can differ in orders of magnitudes for different systems. For example, $\mathrm{Re} \approx 10^4$ for a human swimming in water, whereas $\mathrm{Re} \approx 10^{-4}$ for a microorganism of about 2μm in size [45].

For problems on a micro- to mesoscopic length scale, such as the dynamics of a polymer embedded in a solution, the *Reynolds number* is small enough in order to allow us to neglect the nonlinear advective term $\frac{\rho u L}{\eta}(\boldsymbol{v}\cdot\boldsymbol{\nabla})\boldsymbol{v}$ in the *Navier–Stokes equation* (3.18). The resulting equation is known as the *linearized Navier–Stokes equation*[1]

$$\rho\frac{\partial \boldsymbol{v}}{\partial t} = -\nabla p + \eta\Delta\boldsymbol{v} + (\zeta + \frac{1}{3}\eta)\boldsymbol{\nabla}(\boldsymbol{\nabla}\cdot\boldsymbol{v})\,. \tag{3.24}$$

In some cases, a small *Reynolds number* also justifies dropping the temporal acceleration term $\frac{\rho L^2}{\eta\tau}\frac{\partial \boldsymbol{v}}{\partial t}$ in equation 3.22, resulting in the *creeping flow limit* or *Stokes equation*

$$-\nabla p + \eta\Delta\boldsymbol{v} + (\zeta + \frac{1}{3}\eta)\boldsymbol{\nabla}(\boldsymbol{\nabla}\cdot\boldsymbol{v}) = 0\,. \tag{3.25}$$

However, neglecting temporal acceleration corresponds to resolving on a timescale big enough such that hydrodynamics relax instantaneously to forces local in time.

[1] It should be noted that making a linear expansion in ρ and $\boldsymbol{v}$, i.e. substituting $\rho = \rho_0 + \delta\rho$ and $\boldsymbol{v} = \delta\boldsymbol{v}$, and neglecting terms quadratic in $(\delta\rho, \delta\boldsymbol{v})$ also leads to the *linearized Navier–Stokes equation*.

Chapter 4

Multiparticle Collision Dynamics

Multi-particle Collision Dynamics (MPC) is a particle-based simulation method for hydrodynamic problems. Its first variant was introduced by Malevanets and Kapral in 1999 [46, 47] and has since been developed in different ways to deal with a broad variety of physical systems, starting from macromolecules in simple solvents [48] and fluids with complex boundary conditions such as membranes [49] to viscoelastic fluids [50].

In Multi-particle Collision Dynamics, the fluid is composed of a number of $N \in \mathbb{N}^+$ point-like particles, each of which corresponds to a volume of the fluid that is big compared to a single fluid molecule but small compared to the system size $V = L_x L_y L_z$. The MPC procedure consists of to consecutive phases — a *streaming* phase, in which the particles move ballistically and independent of each other, and a *collision* phase, in which the interaction of the particles is simulated such that the long term behaviour of the fluid obeys the Navier-Stokes equation [51, 52, 53].

4.1 Stochastic Rotation Dynamics

In the *streaming* step, each particle is propagated in time according to ballistic motion:

$$\boldsymbol{r}_i(t + \Delta t) = \boldsymbol{r}_i(t) + \boldsymbol{v}_i(t) \cdot \Delta t \tag{4.1}$$

If the system is constrained by certain boundaries (see section 4.5)— such as walls, periodic boundary conditions, etc. —, their effects would have to be implemented directly after the *streaming* step or in some cases the streaming step would have to be altered altogether. In the subsequent *collision* step, the system is divided into N_{cell} cubic cells with lattice constant a. This length is usually a typical size of the system and has to be chosen carefully (see section 5.1). Each particle is then assigned to a specific cell based on its current position within the system. The cells are then treated independent of each other and the particles

inside a cell interact and exchange momentum with each other in a way that conserves total linear momentum, mass and energy.

The most common procedure that fulfils these conditions is to apply a stochastic rotation on the relative particle velocities (which is why MPC is also known under *Stochastic Rotation Dynamics*) [54],

$$\begin{aligned}\boldsymbol{v}_i(t+\Delta t) &= \boldsymbol{v}_i(t) + (\mathbf{R}(\beta) - \mathbb{1})\,(\boldsymbol{v}_i(t) - \boldsymbol{v}_{cm}(t)) \\ &= \boldsymbol{v}_{cm}(t) + \mathbf{R}(\beta)\,(\boldsymbol{v}_i(t) - \boldsymbol{v}_{cm}(t))\end{aligned} \tag{4.2}$$

where $\boldsymbol{v}_{cm}$ is the center-of-mass velocity of the specific cell, i.e.

$$\boldsymbol{v}_{cm} = \frac{\sum_{i\in cell} m_i \boldsymbol{v}_i}{\sum_{i\in cell} m_i} = \frac{1}{N_c}\sum_{i\in cell} \boldsymbol{v}_i \tag{4.3}$$

The latter holds only if all particles considered have the same mass.

The operator $\mathbf{R}(\beta)$ describes a rotation by an angle β (which is fixed throughout the simulation) around an axis pointing in the direction of a unit vector $\boldsymbol{r} = (r_x, r_y, r_z)^T$, which is chosen randomly for each cell j and each step by uniformly sampling from a 2-sphere $\mathbb{S}^2$ of radius 1. This can be achieved by drawing two numbers $\phi \in [0, 2\pi]$ and $\vartheta \in [-1, 1]$ from uniform distributions of the given intervals and transforming them as follows to yield the components r_α of the unit vector $\boldsymbol{r}$

$$r_x = \sqrt{1-\vartheta^2}\cos\phi \tag{4.4}$$

$$r_y = \sqrt{1-\vartheta^2}\sin\phi \tag{4.5}$$

$$r_z = \vartheta \tag{4.6}$$

Defining $c = \cos\beta$ and $s = \sin\beta$, the rotation operator takes on the form

$$\mathbf{R}(\beta) = \begin{pmatrix} r_x^2 + (1-r_x^2)c & r_x r_y(1-c) - r_z s & r_x r_z(1-c) + r_y s \\ r_x r_y(1-c) + r_z s & r_y^2 + (1-r_y^2)c & r_y r_z(1-c) - r_x s \\ r_x r_z(1-c) - r_y s & r_y r_z(1-c) + r_x s & r_z^2 + (1-r_z^2)c \end{pmatrix} \tag{4.7}$$

Malevanets and Kapral have found an H-theorem for this algorithm, stating that the equilibrium distribution of particle velocities is Maxwellian as well as that the correct hydrodynamic behaviour is produced [46].

4.2 Grid Shift

In its original form, a fixed grid was used to sort the particles into cells at each time-step. However, this procedure renders the algorithm non-Galilean invariant. This effect is

most pronounced if the particles' mean free path $\lambda = \Delta t\sqrt{k_b T/m}$ is small compared to the lattice constant a, i.e. at small temperatures or small time-steps. The violation of Galilean invariance can easily be illustrated if one considers the build-up of correlations of particles in one cell: When the mean free path is small, particles are less likely to leave their current cell, so they collide with the same particles repeatedly and their states become correlated — violating the assumption of molecular chaos. Consider now an imposed homogeneous flow field $\mathcal{V}$, which corresponds to a moving observer in the opposite direction. Such a field would change the correlations between particles and make the transport properties of the fluid dependent on $\mathcal{V}$ — and thus destroy Galilean invariance.

However, Galilean invariance can easily be restored by using a different grid at each time-step [53, 54]. To achieve this, the grid is shifted by a random vector $\boldsymbol{d}$ with components distributed uniformly in the interval $[-a/2, a/2]$. Note that this is equivalent to shifting the particles in the direction $-\boldsymbol{d}$ before sorting and shifting them back to their original positions after the collision. Due to the random grid shift, particles are now grouped into different collision environments at each time-step and interact with different neighbours.

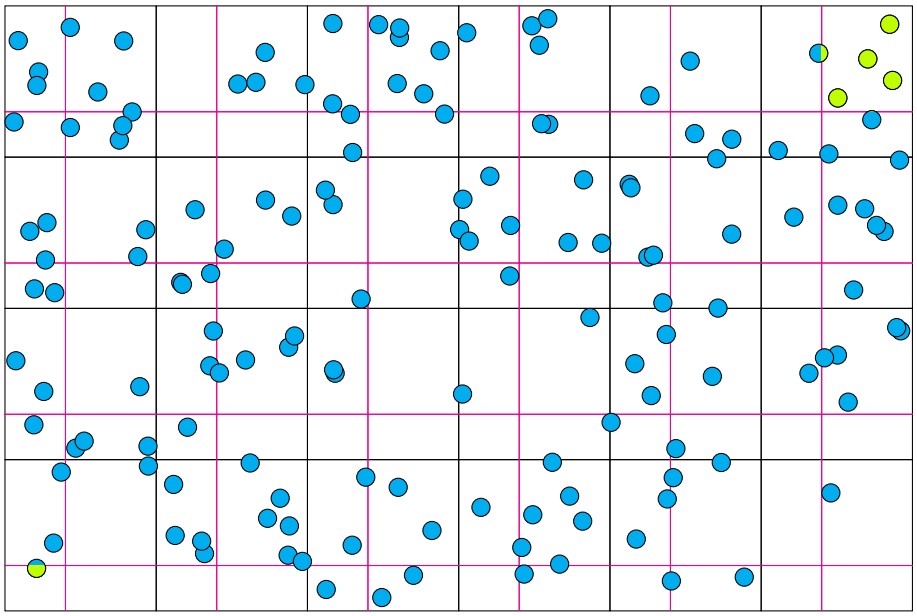

Figure 4.1: Illustration of the grid shift procedure as explained in section 4.2 . Initial cells are coloured black, while shifted cells are coloured purple. The particles belonging to one exemplary box are coloured green to show how boundary conditions are applied.

4.3 Angular Momentum Conservation

It should be noted that the stochastic rotation introduced in section 4.1 does not conserve angular momentum [55]. This leads to an anisotropic stress tensor [56] and non-zero dis-

sipation if the entire fluid is rotated. In most systems this deviation from Navier-Stokes behaviour is negligible, especially in the incompressible fluid limit, where MPC particles move slow compared to the speed of sound. For polymer dynamics, Ripoll *et al.* found excellent agreement between simulations with the SRD algorithm and predictions of the Zimm theory [57].

However, as Götze *et al.* [58] pointed out, there are several situations involving rotating fluids, in which the anisotropy of the stress tensor gives rise to non-physical torques. They were able to identify three cases: (i) boundary conditions defined by torques, (ii) binary fluid mixtures of different viscosities and (iii) polymers with a high local monomer density. It should be noted, however, that in the last case, problems can be avoided if the size of the MPC cells is approximately equal to the excluded volume of the monomers.

Various modifications have been proposed to restore conservation of angular momentum in the SRD algorithm. One possibility is to have the collision angle β depend on the velocities and positions of the particles in a given cell [59]. Another widely used approch is to perform a rigid-body rotation after the collision to compensate for the initial change in angular momentum $\Delta\mathbf{L}$ [60, 61, 62]. The total velocity update during the *collision* phase then reads

$$\boldsymbol{v}_i(t+\Delta t) = \boldsymbol{v}_{cm}(t) + \mathbf{R}(\beta)\left(\boldsymbol{v}_i(t) - \boldsymbol{v}_{cm}(t)\right) + \boldsymbol{\omega} \times \boldsymbol{r}_{i,cm}(t+\Delta t) \tag{4.8}$$

where the angular velocity $\boldsymbol{\omega}$ is

$$\boldsymbol{\omega} = \boldsymbol{\Pi}^{-1} \underbrace{\{ \sum_{i \in \text{cell}} m_i \left[\boldsymbol{r}_{i,cm}(t+\Delta t) \times \left(\boldsymbol{v}_{i,cm}(t) - \mathbf{R}(\beta)\boldsymbol{v}_{i,cm}(t)\right)\right]\}}_{-\Delta\mathbf{L}} . \tag{4.9}$$

Note that all quantities with subscript *i,cm* are in the center-of-mass reference frame of the current cell. For the implementation, one does not invert the moment of inertia tensor $\boldsymbol{\Pi}$, but instead solves the linear equation $-\Delta\mathbf{L} = \boldsymbol{\Pi} \cdot \boldsymbol{\omega}$ for $\boldsymbol{\omega}$.

A downside of this algorithm is that, while conserving angular momentum, it does not conserve energy. Thus, a thermostat has to be added when using this variant of MPC. For the simulation of telechelic star polymers under shear, results for MPC with and without angular momentum conversation were compared for $f = 15$, $\alpha = 0.3$, $\lambda = 1.05$ and different shear rates, but no significant deviations could be observed, so angular momentum conservation was subsequently not incorporated for performance reasons.

4.4 Maxwell-Boltzmann Scaling Thermostat

Since the stochastic rotation variant of MPC conserves energy (cf. section 4.1), it yields statistics corresponding to a microcanonical ensemble. However, in some situations it is

more desirable to simulate at a constant temperature instead of at a constant energy: if thermal fluctuations might lead to new characteristics of a polymer, simulations should be comparable to experiments or in the presence of external fields and viscous heating. For the simulations in this work, the *Maxwell-Boltzmann Scaling* thermostat was used. It is a velocity scaling algorithm acting locally on a cell-level and was first introduced for MPC by Huang *et al.* [63].

In a cell of N_c particles, the set of relative velocities $\{\boldsymbol{v}\} = \{\boldsymbol{v}_{i,cm} | i \in cell\}$ at a given temperature T should be distributed according to the Maxwell-Boltzmann distribution

$$P(\{\boldsymbol{v}\}) = \left(\frac{m}{2\pi k_B T}\right)^{3N_c/2} \exp\left(-\frac{m}{2k_B T} \sum_{i \in cell} \boldsymbol{v}_{i,cm}^2\right) \tag{4.10}$$

From this, we can calculate the probability that the particles of a cell have the local kinetic energy E_k by integrating over all possible sets $\{\boldsymbol{v}\}$ with $\sum_{i \in cell} \frac{m_i}{2} \boldsymbol{v}_{i,cm}^2 = E_k$. The probability density for the local kinetic energy is then given by [64]

$$P(E_k) = \frac{1}{E_k \gamma(f/2)} \left(\frac{E_k}{k_b T}\right)^{f/2} \exp\left(\frac{-E_k}{k_b T}\right) \tag{4.11}$$

Here, $f = 3(N_c - 1)$ denotes the degrees of freedom within a cell and $\gamma(x)$ is the gamma function. Note that this distribution converges to a Gaussian function with mean $\langle E_k \rangle = f k_B T/2$ and variance $(\Delta E_k)^2 = f(k_B T)^2/2$.

For each cell, a new kinetic energy E_k' is drawn randomly from the distribution in equation 4.11 and the particles' relative velocities are scaled by a factor κ

$$\boldsymbol{v}_{i,cm} \to \kappa \boldsymbol{v}_{i,cm} \qquad \text{with} \quad \kappa = \sqrt{\frac{2E_k'}{\sum_{i \in cell} m_i \boldsymbol{v}_{i,cm}^2}} \tag{4.12}$$

so that the new local kinetic energy is E_k'.

4.5 Boundary Conditions and Shear Flow

Since MPC simulations are carried out in finite systems, boundary conditions have to be chosen and implemented to keep the number of particles within the simulation box fixed. As mentioned earlier in this chapter, one advantage of MPC is the great variety of possible boundary conditions that can be implemented alongside with it. These include so-called *slip* [47, 65] and *no-slip boundary conditions* [66], where particles bounce back when they hit the surface and are given a new velocity. The boundary conditions used in this work are *periodic boundary conditions* and *Lees–Edwards boundary conditions*, which will be explained in the following.

4.5.1 Periodic Boundary Conditions

Periodic boundary conditions were introduced for molecular dynamics simulation to lessen the problem of artificial surface effects [67]. Instead of having a finite system, the central box is considered to be replicated periodically in all directions, forming an infinite lattice. Therefore, when a particle leaves the central box in one direction, one of its image particles will enter from the opposite surface. Implementation-wise, this means that a particle's position $\boldsymbol{r}$ will be mapped into the central box according to

$$r_j \to r'_j = r_j - c_j L_j \qquad \text{for } j \in \{x, y, z\} \tag{4.13}$$

where L_j is the side-length of the central box in the j direction. The constant c_j is chosen such that r'_j lies within the boundaries of the box. For a system with its origin at the lower forward left corner, $c_j = \lfloor r_j/L_j \rfloor$[1], such that $r_j \in [0, L_j]$. On the other hand, for a system with its origin at the center of the box, $c_j = \lfloor r_j/L_j \rceil$[1], such that $r_j \in [-L_j/2, +L_j/2]$. In the following, we will always consider the latter choice. In some situations, it may be more desirable to have the particles propagate through the infinite system and only virtually folding them back into the central box for the sorting procedure — for example when calculating dynamic properties of the fluid such as mean-squared displacement. However, one should be aware that such an implementation will decrease the accuracy of the floating point numbers used to store the positions, if the particles move too far from the origin [68].

4.5.2 Lees–Edwards Boundary Conditions

Lees–Edwards boundary conditions are a method to combine shear flow with periodic boundary conditions [69, 25, 50]. The infinte system considered when using periodic boundary conditions (cf. 4.5.1) is subjected to a uniform shear in the $x - y$ plane with shear rate $\dot{\gamma} = \frac{\mathrm{d}v_x}{\mathrm{d}r_y}$. The layer of boxes whose centers are at $(x, 0, z)$ are stationary, while layers above and below move with a contant velocity of $\boldsymbol{v}_{box} = (\pm\dot{\gamma}L_y, 0, 0)$ (see figure 4.2). Therefore, when a particle leaves the central box in the y direction, one of its images will enter the central box from the opposite surface, but since the image box from which it enters is displaced by a factor $\mathrm{d}x = \dot{\gamma}L_y t$ in the x-direction, the image particle will enter the center box also displaced that way. Additionaly, it will have a x-velocity that is smaller than the original

[1]Here, $\lfloor\ \rfloor$ denotes mapping to the largest previous integer, $\lceil\ \rceil$ denotes mapping to the smallest following integer and $\lfloor\ \rceil$ denotes mapping to the nearest integer.

particle by $\dot{\gamma}L_y$. Mathematically, these boundary conditions can be expressed as

$$
\begin{aligned}
r_x \to r'_x &= r_j - \lfloor \frac{r_y}{L_y} \rceil \dot{\gamma} L_y t \\
v_x \to v'_x &= v_x - \lfloor \frac{r_y}{L_y} \rceil \dot{\gamma} L_y \\
r_j \to r'_j &= r_j - \lfloor \frac{r_j}{L_j} \rceil L_j \qquad \text{for } j \in \{x, y, z\}
\end{aligned}
$$

[1]

Note that periodic boundary conditions are recovered in the case of $\dot{\gamma} = 0$.

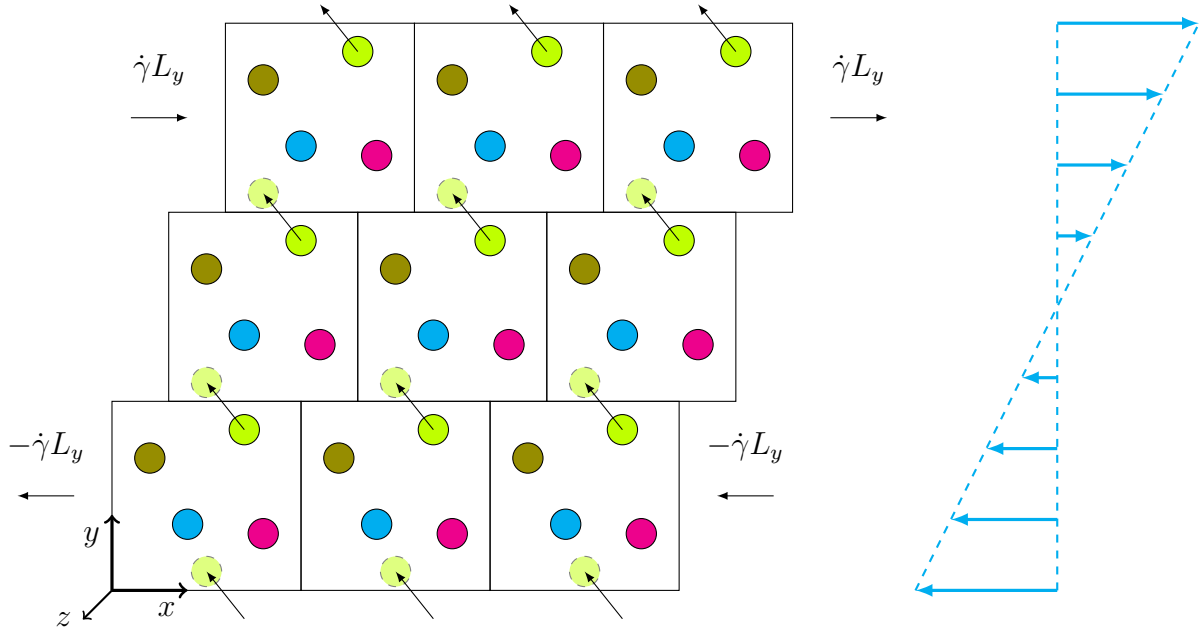

Figure 4.2: Lees–Edwards boundary conditions for homogeneous shear flow. The green spheres demonstrate what happens when a particle leaves the central box and boundary conditions are applied. The blue arrows indicate the average velocity profile of the fluid.

4.6 Embedded Objects

Macromolecules such as colloids or polymers can easily be incorporated into the MPC algorithm by including them as point particles in the *collision* step [48]. For monomers of mass M and velocities $\boldsymbol{V}_i$, the center-of-mass velocity in equation 4.2 is then calculated according to

$$
\boldsymbol{v}_{cm} = \frac{m \sum_{i \in cell}^{N_c} \boldsymbol{v}_i + M \sum_{i \in cell}^{N_m} \boldsymbol{V}_i}{N_c m + N_m M} \tag{4.14}
$$

where N_m is the number of monomers in a given cell. During the stochastic collision, the monomers and the MPC particles exchange momenta. This interaction is generally strong enough to keep embedded objects at a desired temperature by introducing a thermostat for the fluid particles only. Between successive collisions monomers are propagated in time

according to their equations of motion by a molecular dynamics scheme of time-step Δt_{MD}, which is usually much smaller than the time-step Δt of the MPC routine.

When embedding polymers in an MPC fluid, the average number of monomers per cell $\langle N_m \rangle$ should not be greater than unity, so that hydrodynamic interactions between neighbouring monomers can build up. Therefore, the lattice constant a should be chosen to be of the order of the average bond length of the polymer, provided the monomers are also subjected to excluded volume interactions, which is the case here. Furthermore, the mass of the monomers should match the average mass of fluid particles per cell [70], i.e. $M = \langle N_c \rangle m$.

4.7 Verification of the Algorithm

In the following section, a few static and dynamic properties of the *MPC* fluid will be tested against both analytical and published results to ensure the correctness of the implementation.

Unless stated otherwise, the parameters used in these preliminary simulations were chosen as follows. The primary box had dimensions $L_x = L_y = L_z = 30a$, with $a = 1.0$, and the average number of particles per cell was $\langle N_c \rangle = 10$ – which amounts to a total of $N = \frac{L_x L_y L_z}{a^3} \langle N_c \rangle = 270000$ particles. The rotation angle β was set to 130° and the time-step to $\Delta t = 0.1\sqrt{ma^2/k_B T}$. Finally, the system was simulated at a temperature of $k_B T = 1$.

4.7.1 Velocity Distribution

First of all, the correct implementation of the *Maxwell–Bolzmann Scaling Thermostat* (cf. section 4.4) was tested. Figure 4.3 shows the probability density of absolute velocities averaged over all *MPC* particles. The results are in excellent agreement with the theoretical prediction based on the Maxwell–Boltzmann distribution (4.10).

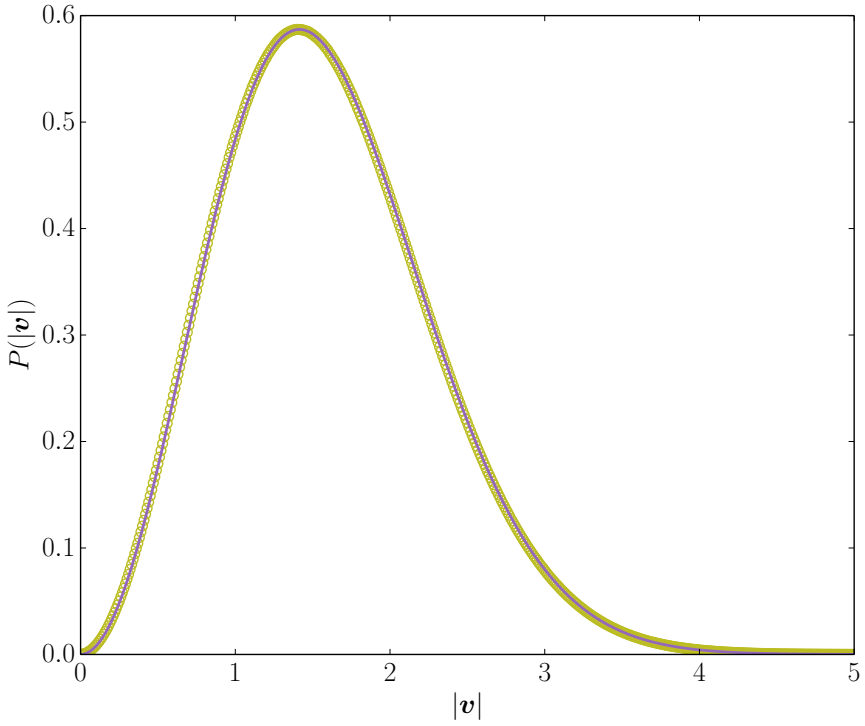

Figure 4.3: Distribution of absolute velocities averaged over all MPC particles for a temperature of $T = 1$ and without shear. Circles represent simulation results while the solid line shows the theoretical prediction based on the Maxwell–Boltzmann distribution.

4.7.2 Velocity-Autocorrelation Function

In order to verify the implementation of the *MPC* algorithm, it is instructive to take a look at velocity autocorrelation functions. It has been shown [46, 47, 55, 56] that the *MPC* fluid exhibits the correct hydrodynamic behaviour according to the linearized Navier-Stokes equations on sufficiently large length and time scales (see section 3.4). Therefore, it is possible to derive analytical expressions for the velocity autocorrelation functions by solving the linearized Navier-Stokes equations in Fourier space by applying the following transformations

$$\boldsymbol{v}(\boldsymbol{r},t) = \frac{1}{2\pi}\sum_k \int \hat{\boldsymbol{v}}(\boldsymbol{k},\omega)\, e^{-i\boldsymbol{k}\cdot\boldsymbol{r}}\, e^{i\omega t}\mathrm{d}\omega \tag{4.15}$$

$$\hat{\boldsymbol{v}}(\boldsymbol{k},\omega) = \frac{1}{V}\int \boldsymbol{v}(\boldsymbol{r},t)\, e^{i\boldsymbol{k}\cdot\boldsymbol{r}}\, e^{-i\omega t}\mathrm{d}^3 r\mathrm{d}t \tag{4.16}$$

with $k_\alpha = 2\pi n_\alpha / L$ and $n_\alpha \in \mathbb{Z} \setminus \{0\}$.

Splitting the velocity in fourier space $\hat{\boldsymbol{v}}$ into a longitudinal $\hat{\boldsymbol{v}}^L$ and a transverse part $\hat{\boldsymbol{v}}^T$ with respect to $\boldsymbol{k}$, we can find analytical expressions for the velocity autocorrelation functions of both parts, i.e.

$$\langle \boldsymbol{v}^T(\boldsymbol{k},t)\cdot\boldsymbol{v}^T(-\boldsymbol{k},0)\rangle = \frac{2k_BT}{\rho V}e^{-\nu k^2|t|} \tag{4.17}$$

and

$$\langle \boldsymbol{v}^L(\boldsymbol{k},t)\cdot\boldsymbol{v}^L(-\boldsymbol{k},0)\rangle = \begin{cases} \frac{k_BT}{\rho V}e^{-\tilde{\nu}k^2|t|/2}\left[\cos(\Omega|t|)-\sqrt{\frac{k^2\tilde{\nu}^2}{4c^2-k^2\tilde{\nu}^2}}\sin(\Omega|t|)\right], & \text{if } \frac{4c^2}{k^2\tilde{\nu}^2}>1\,, \\ \frac{k_BT}{\rho V}e^{-\tilde{\nu}k^2|t|/2}\left[\cosh(\Lambda|t|)-\sqrt{\frac{k^2\tilde{\nu}^2}{k^2\tilde{\nu}^2-4c^2}}\sinh(\Lambda|t|)\right], & \text{if } \frac{4c^2}{k^2\tilde{\nu}^2}<1\,, \end{cases} \tag{4.18}$$

where $\nu=\eta/\rho$, $\tilde{\nu}=\tilde{\eta}/\rho=(\eta+\eta_k/3)/\rho$, $\Omega=k^2\tilde{\nu}\sqrt{4c^2/(k^2/\tilde{\nu}^2)-1}/2$ and $\Lambda=k^2\tilde{\nu}\sqrt{1-4c^2/(k^2/\tilde{\nu}^2)}/2$.

The velocity correlation function in real space follows by applying the inverse Fourier transformation

$$\langle \boldsymbol{v}(\boldsymbol{r},t)\cdot\boldsymbol{v}(\boldsymbol{r}',0)\rangle = \sum_k \langle \boldsymbol{v}(\boldsymbol{k},t)\cdot\boldsymbol{v}(-\boldsymbol{k},t)\rangle e^{-i\boldsymbol{k}\cdot(\boldsymbol{r}-\boldsymbol{r}')}\,, \tag{4.19}$$

where $\langle \boldsymbol{v}(\boldsymbol{k},t)\cdot\boldsymbol{v}(-\boldsymbol{k},t)\rangle$ is the sum of the longitudinal and two times the transverse autocorrelation functions. For a detailed derivation the interested reader is referred to appendix A.

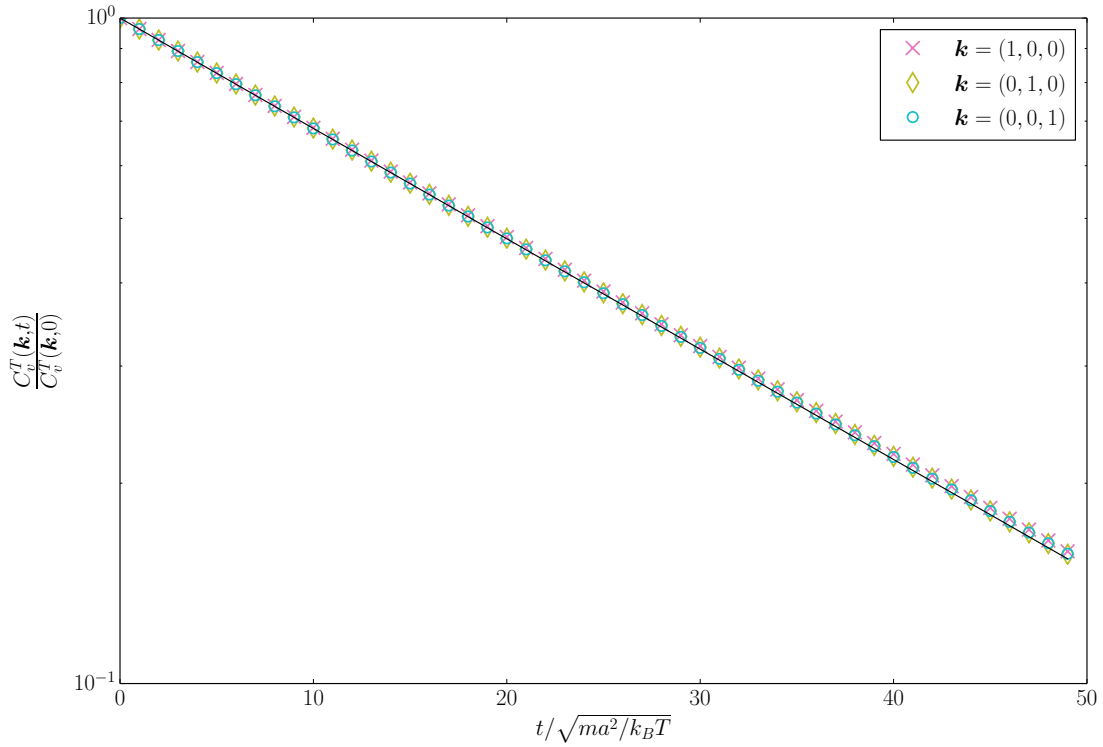

Figure 4.4: Normalized transverse velocity autocorrelation function for different values of $\boldsymbol{k}$. The symbols represent simulation data, whereas the solid line represents the analytical expression.

Figure 4.4 displays the results for the transverse velocity autocorrelation for three different values of $\boldsymbol{k}$, corresponding to the three spatial dimensions in Fourier space. Since the three curves collapse onto each other over the whole time-period sampled, one can assume that the fluid is isotropic as expected. Furthermore, excellent agreement with the theoretical prediction (equation 4.17) for a kinematic viscosity of $\nu = 0.87$ is achieved.

4.7.3 Homogeneous Shear Flow

Applying *Lees–Edwards boundary conditions* introduces homogeneous shear into the system (cf. section 4.5.2). The fluid should respond to this by developing a linear velocity profile in the $x - y$ plane

$$v_x = \dot{\gamma} y \tag{4.20}$$

We tried to verify this behaviour by dividing the box in the y-direction into small slices of length 0.2 and averaging over the velocities in the x-direction v_x of all particles in a given slice over the course of the simulation. The results are presented in figure 4.5 and exhibit excellent agreement with the theoretical prediction.

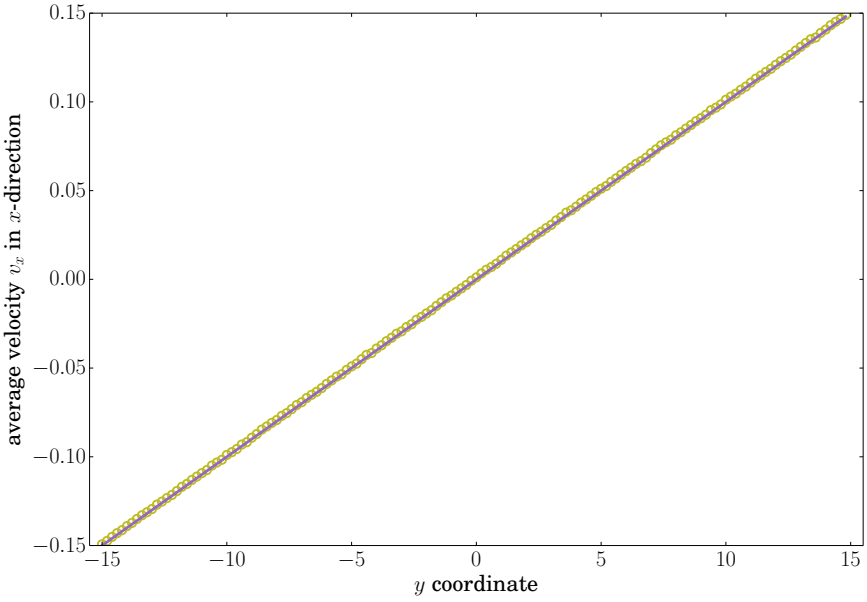

Figure 4.5: Velocity profile of a MPC fluid with Lees–Edwards boundary conditions

Chapter 5

Telechelic Star Polymers under Shear

In the present chapter, the implementation and choice of parameters for the simulation will be explained and the results for the characteristics described in chapter 2 will be presented.

5.1 Implementation and Simulation Parameters

To investigate the behaviour of telechelic star polymers under the presence of a homogeneous shear flow we used a hybrid simulation technique that combines molecular dynamics (MD) with multiparticle collision dynamics (MPC). The monomers of the telechelic star polymer are propagated in time according to their Newtonian equations of motion with the help of the Velocity-Verlet integration scheme [71, 72]. Let $\boldsymbol{r}_i(t)$ and $\boldsymbol{v}_i(t)$ be the position and velocity of the ith monomer at time t, and let $\boldsymbol{F}_i(t)$ be the sum of all pairwise additive forces acting on given monomer. Then, the updated positions $\boldsymbol{r}_i(t+\Delta t)$ and velocities $\boldsymbol{v}_i(t+\Delta t)$ after a time step of Δt are calculated as follows

$$\boldsymbol{r}_i(t+\Delta t) = \boldsymbol{r}_i(t) + \boldsymbol{v}_i(t)\Delta t + \frac{\boldsymbol{F}_i(t)}{2m}\Delta t^2\,, \tag{5.1}$$

$$\boldsymbol{v}_i(t+\Delta t) = \boldsymbol{v}_i(t) + \frac{1}{2m}\left(\boldsymbol{F}_i(t) + \boldsymbol{F}_i(t+\Delta t)\right)\Delta t\,. \tag{5.2}$$

Since we need the forces at time t and $t+\Delta t$, we have to make a force calculation after updating the positions of all particles and before updating the velocities of all particles.

To speed up the force calculations, Verlet lists [71, 72] for each monomers are kept, indicating the neighbours of each monomer within a certain cut-off distance r_v – which is chosen slightly larger than the cut-off for the force calculation r_c. To construct and update these lists, the simulation box is divided into smaller sub-boxes of length r_c, such that only particles belonging to one of the 27 neighbouring sub-boxes have to be checked for finding the members of one monomer's Verlet list [73]. These neighbour lists have to be updated

whenever any monomer has travelled a distance greater or equal to $r_v - r_c$ since the last update.

The star polymer was coupled to the MPC solvent by including it in the stochastic rotation as described in section 4.6. Unless stated otherwise, the parameters used in the final simulations were chosen as follows. For the solvent particles a time-step of $\Delta t_s = 0.1$ was used, while the motion of the monomers of the star polymers was integrated using a smaller time-step of $\Delta t_m = 0.001$. The side length of the MPC cells must be chosen such that there is approximately one monomer per cell in order to properly resolve hydrodynamic interactions while also capturing the effects of anisotropic friction. Since the bond length of the monomers is $b \approx 1$, we chose $a = 1.0$ as the side length of the cells to ensure this. The rotation angle β was set to 130° and the system was simulated at a temperature of $k_B T = 0.5$. Note that all simulation parameters not specific to the solvent were the same as for the equilibrium simulations described in section 2.2. In terms of star architecture, stars of 6, 9 and 15 arms with amphiphilicities α of 0.3 and 0.5 were investigated. The attraction coupling constant λ was varied between 0.5 and 1.15.

In the following sections, the behaviour of star polymers will be discussed separately for the two different amphiphilicities investigated in our simulations, $\alpha = 0.3$ and $\alpha = 0.5$, respectively.

5.2 The Case of Low Amphiphilicity $\alpha = 0.3$

As discussed earlier in section 2.2, in equilibrium, stars of an amphiphilicity as low as $\alpha = 0.3$ form patches whose number and size is a monotonically increasing function of the attraction coupling constant (or inverse temperature) λ for all the values of λ considered here (i.e. $\lambda \leq 1.15$). Furthermore, in this range, the attraction between B-type monomers is not strong enough to form any patches of more than two arms (see figures 2.2a and 2.3a). Since athermal star polymers elongate and take on a more prolate shape under linear shear conditions [74], we would expect that applying shear on end-functionalised star polymers promotes clustering and leads to an increase in patch size and a stabilisation of patches at lower values of λ than in equilibrium conditions.

5.2.1 Characterization of Patchiness

Figure 5.1 shows the number of patches N_p (left column) as well as the size of the formed patches s_p (right column) for 6 (top), 9 (middle) and 15 (bottom) arms and various inverse temperatures λ as a function of the dimensionless Weissenberg number Wi ranging from 0 to $\approx 10^3$. For all functionalities considered, the stars seem to make a transition from

a constant number of patches to a monotonic increase with Weissenberg number. This transition happens at lower shear rates at lower temperature and higher functionality.

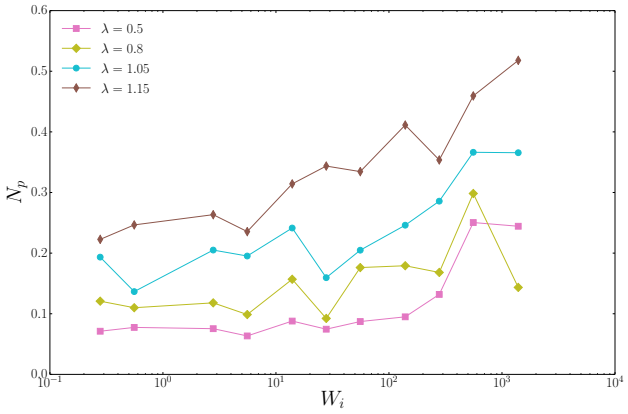

(a) $f = 6$

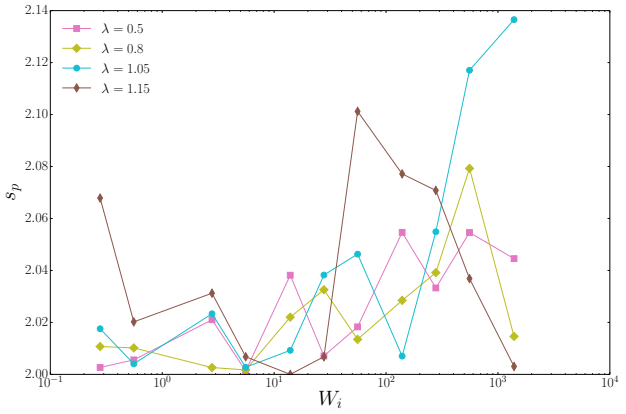

(b) $f = 6$

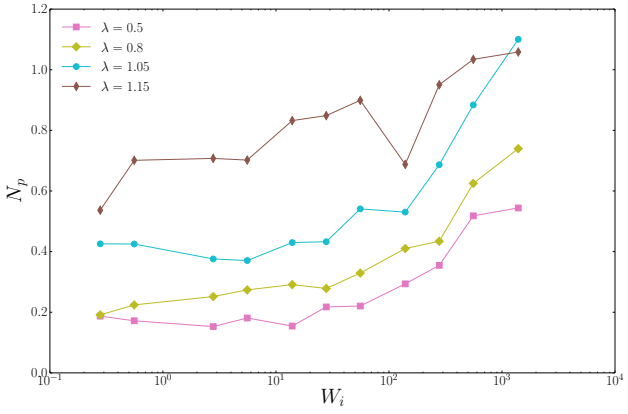

(c) $f = 9$

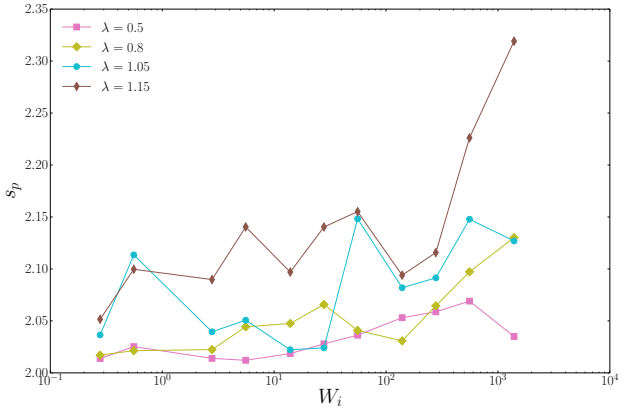

(d) $f = 9$

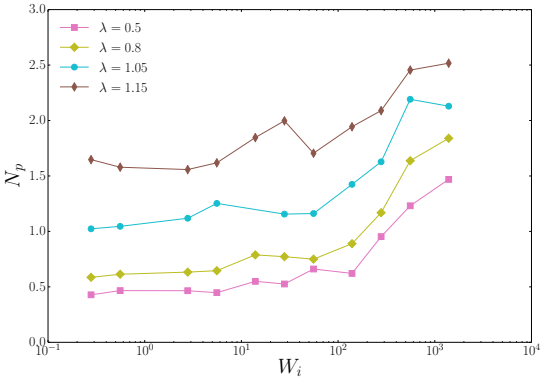

(e) $f = 15$

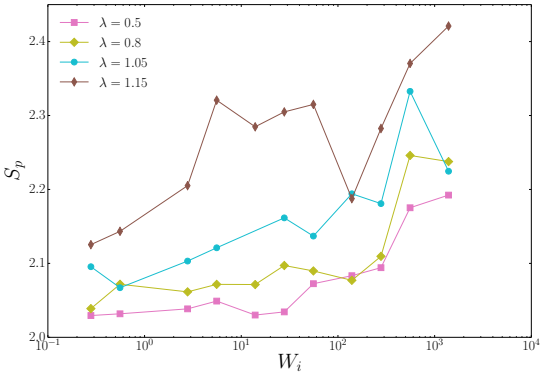

(f) $f = 15$

Figure 5.1: Number of patches N_p (left) and patch-size s_p (right) as a function of Weissenberg number Wi for functionalities $f \in \{6, 9, 15\}$ (from top to bottom) and amphiphilicity $\alpha = 0.3$

Even though the change with increasing shear rate is quite similar for stars of different functionalities, the range between the minimum and the maximum number of patches for

a given star architecture is quite different depending predominantely on functionality. On the end of very low functionality, $f = 6$, the average number of patches is always below 1, indicating that either the lifetime of two-arm patches is increased by high shear or that patches are formed more often at high shear. To find out which of those two assumptions is true, we examined the conformations of such stars at different shear rates in more detail.

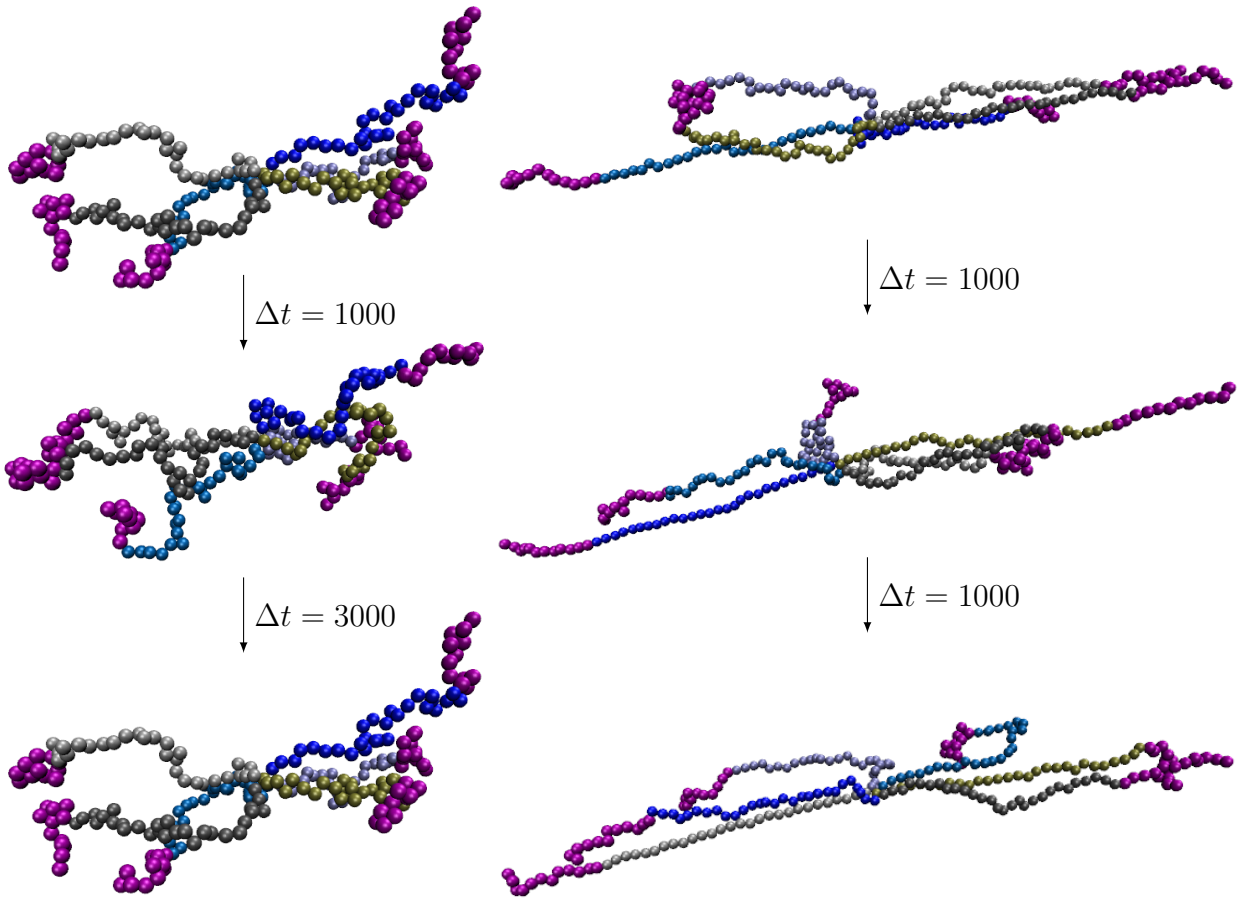

(a) Wi ≈ 30 (b) Wi ≈ 560

Figure 5.2: Representative conformations of a TSP with $f = 6$, $\alpha = 0.3$ and $\lambda = 1.05$ at an intermediate (Wi ≈ 30, left) and a high shear rate (Wi ≈ 560, right). Purple spheres correspond to solvophobic B-type monomers, while solvophilic A-type monomers are coloured in different shades of grey and blue according to which arm they belong to.

Figure 5.2 shows consecutive snapshots of a star with six arms at an inverse temperature of $\lambda = 1.05$ at an intermediate (left) and a high (right) Weissenberg number. We notice that at high shear rates, arms change from one side to the other relatively often. This might be responsible for the quick formation and breaking of patches, as can be seen from the shorter lifetime of the patch between the two grey arms at Wi ≈ 560 than at Wi ≈ 30 (middle configurations). These faster dynamics at high shear rates could be observed throughout

the whole simulation. Thus, we can conclude that for stars of low functionality and low amphiphilicity, shear makes patches less stable but at the same time more abundant.

For stars of high functionality, $f = 15$, on the other hand, the changes in *patchiness* with increasing shear rate are qualitatively more diverse than in the low functionality case. For $\lambda = 1.05$, for example the average number of patches changes from one in equilibrium to two at high Weissenberg numbers. Interestingly, however, for even higher attraction between solvophobic monomers, $\lambda = 1.15$, the star structure changes from one or two patches forming in equilibrium to two or three patches forming at the highest shear rate considered. The ability to form three patches when subjected to high shear flows is intriguing, since intuitively one would assume that the elongation induced by the linear velocity profile would promote the formation of two patches at the ends of the prolate ellipsoidal shape. Comparing the conformations at intermediate and high shear rates (figures 5.3a and 5.3b, respectively), we notice that the two patches formed at the left end of the star at high shear rate are in fact very close to each other. However, the attraction between them is not high enough to get them to collapse onto each other. Furthermore, arms forming patches seem to be much shorter than free arms at high shear due to the clustering of the solvophobic monomers and the steric repulsion between the solvophilic monomers. Elongated free arms between patches might thus hinder the collapse of several patches onto one.

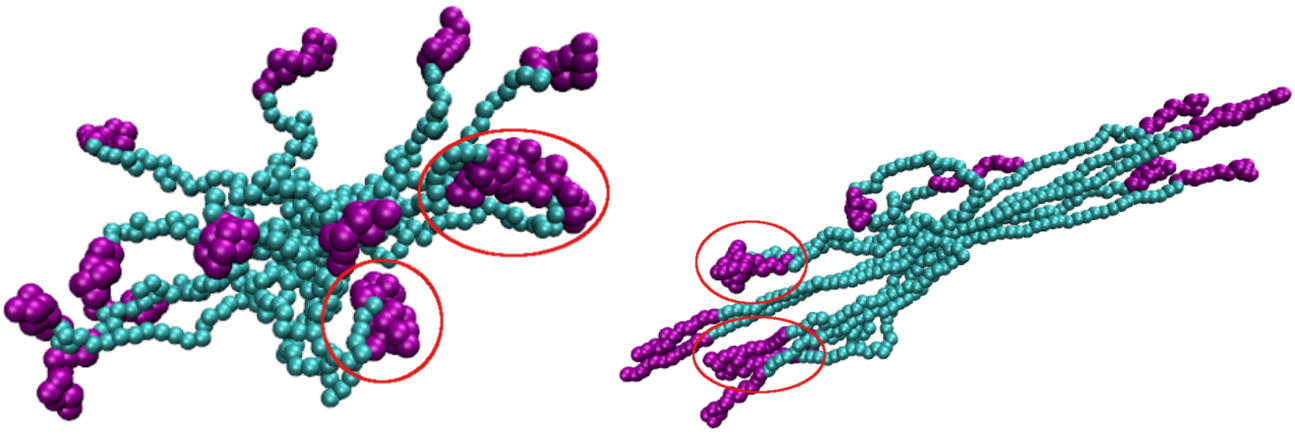

(a) Wi ≈ 50 (b) Wi $\approx 10^3$

Figure 5.3: Representative conformations of a TSP with $f = 15$, $\alpha = 0.3$ and $\lambda = 1.15$ at an intermediate (Wi ≈ 50, left) and a high shear rate (Wi $\approx 10^3$, right). Purple spheres correspond to solvophobic B-type monomers, while solvophilic A-type monomers are coloured in blue. Patches formed are marked by red ellipses.

5.2.2 Conformation and Shape Parameters

The results obtained so far all depend upon our specific definition of a patch, which is computed via a threshold-based clustering algorithm as explained in section 2.2.1. When using such techniques one should always bear in mind that they have an intrinsic ambiguity associated with them and small differences in the definition of a patch might lead to qualitative different results. To compensate for this problem, we also characterise the conformation of the telechelic star polymers in terms of their gyration tensor and calculate the shape parameters *prolateness* and *acylindricity* derived from it (*cf.* section 2.2.2). If we can relate these measures of star shape along with the visual inspections of the conformations to our results about the patch formation, we can confirm that our definition of a patch is self-consistent.

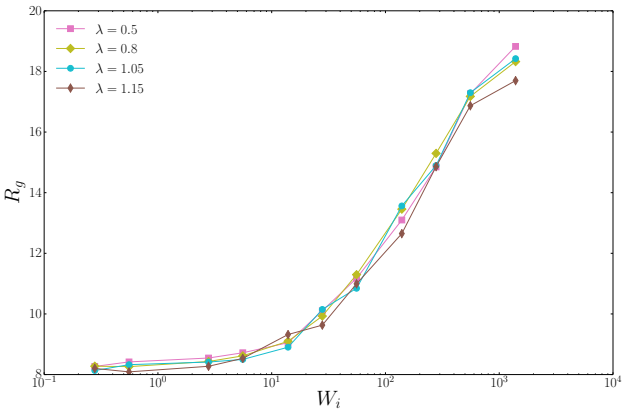

(a) $f = 6$

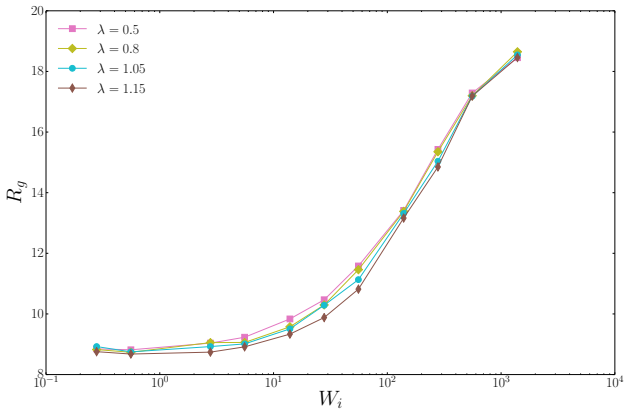

(b) $f = 9$

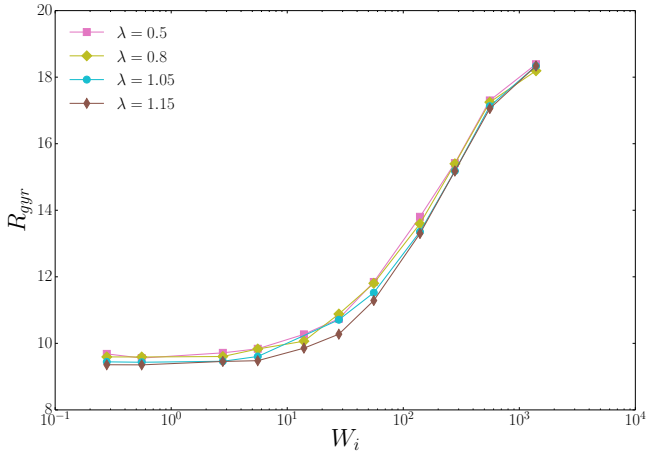

(c) $f = 15$

Figure 5.4: Radius of gyration R_g as a function of Weissenberg number Wi for functionalities $f \in \{6, 9, 15\}$ (from left to right and top to bottom) and amphiphilicity $\alpha = 0.3$

We start by analysing the radius of gyration R_g, which is the least sensitive measure of shape, since it only gives a rough estimate about the overall size of the molecule. Figure 5.4 shows the radius of gyration as a function of Weissenberg number for all functionalities considered. As already seen in the snapshots of the configurations (*cf.* figures 5.3), the radius of gyration increases drastically with increasing shear rate after a certain threshold on the order of Wi ≈ 10, which is approximately the same for all functionalities. Although not visible in the case of six arms, the radius of gyration is smaller for higher λ, especially at intermediate shear rates. This could be due to the resistance against elongation of arms which are part of a patch, as was discussed in the previous section and seen in figure 5.3b.

The elongation of the stars with shear rate is also demonstrated by the prolateness S, depicted in the left column of figure 5.6. However, contrary to the behaviour of the gyration radius, we notice no dependence of the prolateness on the attraction coupling constant λ. According to the definition of the prolateness in equation 2.11, it depends on the relative differences between the eigenvalues of the gyration tensor. Looking at the conformation of stars with different values of λ at the same Weissenberg number (figure 5.5), we notice that while arms in patches are less elongated, a star with more patches also has less free arms which can increase the extension of the star perpendicular to the axis of the largest eigenvalue. Therefore, these two effects might compensate each other in a way that the prolateness is independent of the attraction between B-monomers.

Finally, we turn to an examination of the acylindricity c (right column of figure 5.6). It drops drastically at high shear rates, which is not surprising, given that the undisturbed velocity field is symmetric with respect to a rotation around the direction of its gradient. As the molecule aligns itself with the flow it should at least partially adopt this symmetry, which leads to a convergence of the two smallest eigenvalues of the gyration tensor and thus an acylindricity going to zero.

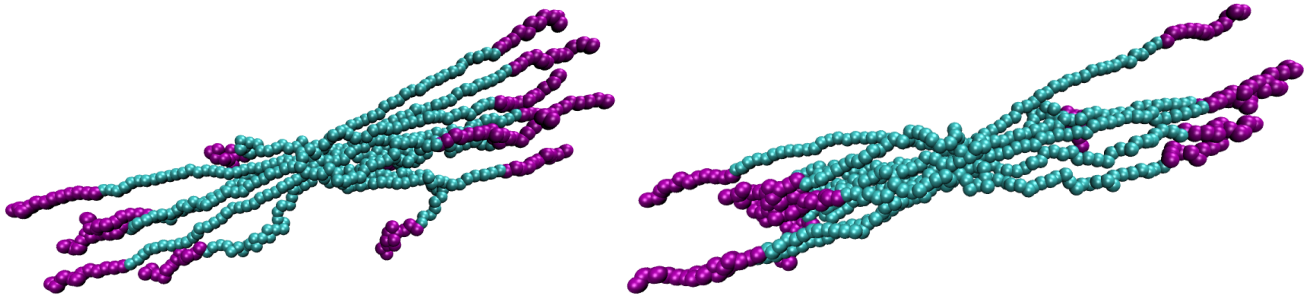

(a) $\lambda = 0.8$ (b) $\lambda = 1.15$

Figure 5.5: Representative conformations of a TSP with $f = 15$ with different interaction strengths λ at a high shear rate with Wi ≈ 500. Purple spheres correspond to solvophobic B-type monomers, while solvophilic A-type monomers are coloured in blue.

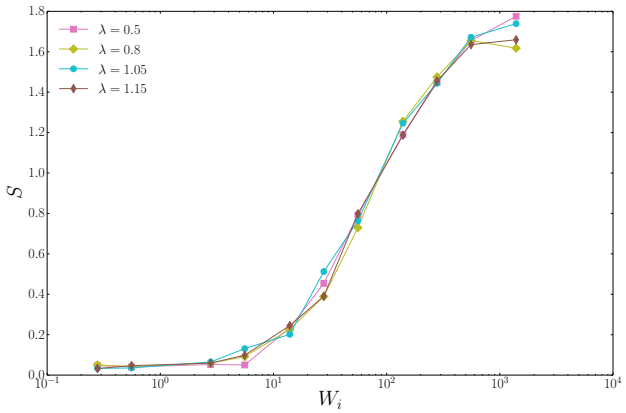

(a) $f = 6$

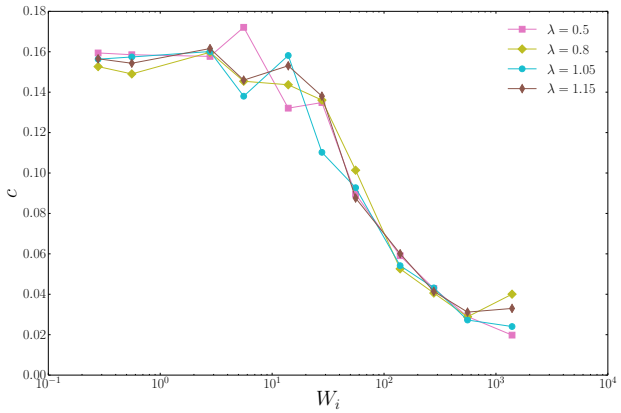

(b) $f = 6$

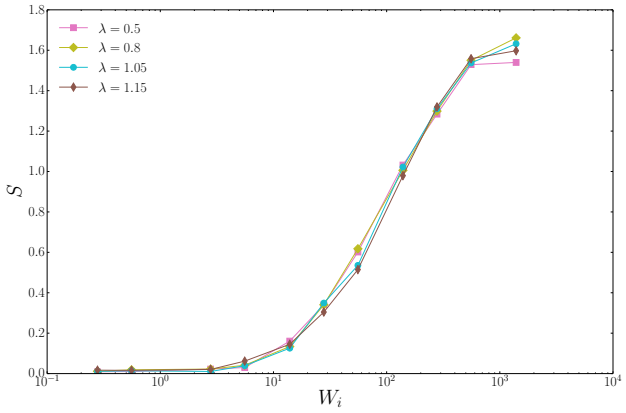

(c) $f = 9$

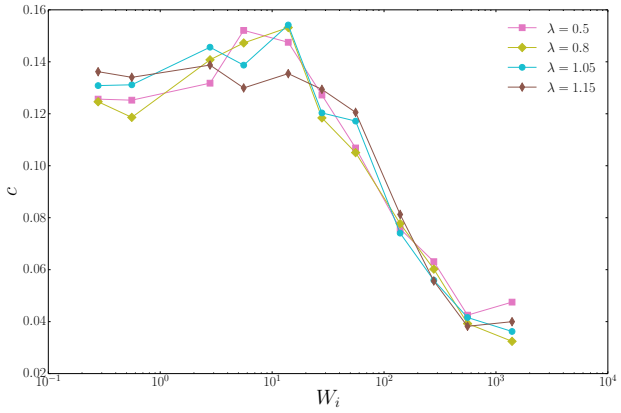

(d) $f = 9$

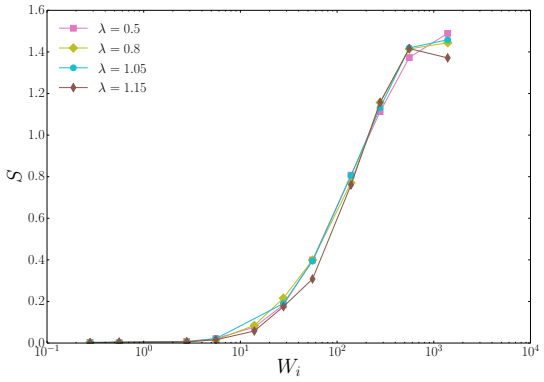

(e) $f = 15$

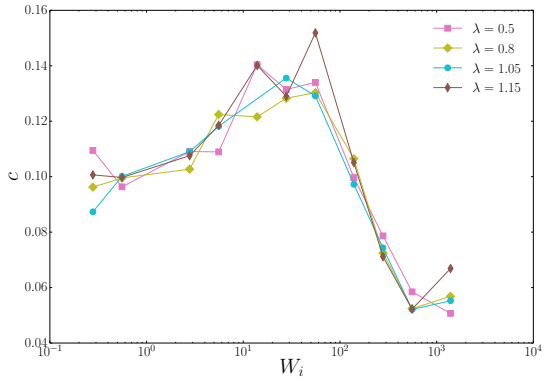

(f) $f = 15$

Figure 5.6: Prolateness S (left) and acylindricity c (right) as a function of Weissenberg number Wi for functionalities $f \in \{6, 9, 15\}$ (from top to bottom) and amphiphilicity $\alpha = 0.3$

However, we do not see any trend with respect to λ – for a given functionality, all the curves collapse onto each other within the statistical error. The different trends for different functionalities seem to stem from the fact that for intermediate to high shear rates, all stars undergo the same transition from low to high cylindrical symmetry, but their equilibrium

conformations vary significantly, with stars of high functionality being more cylindrical than those of low functionality. The conformations of figure 5.7 illustrate the non-monotonicity of the acylindricity for stars of fifteen arms. The figure shows a star with $\lambda = 1.05$ and functionality $f = 15$ at low, intermediate and high shear rates, respectively. Each conformation is viewed in two different planes – the flow-gradient plane above and the flow-vorticity plane below – to compare the extension of the star in different directions. For small shear rates, the TSP assumes a highly spherical shape and thus exhibits a small acylindricity. As the shear gets stronger, the star is stretched in the flow direction while an extension in the gradient direction is hinderes, leading to an increase in acylindricity. At high shear rates, extension in the vorticity direction is inhibited as well, with the exception of the occasional arm rotating in the flow-vorticity plane in the course of the TSP's tank-treading motion. Furthermore, at high shear rates the acylindricity is less sensitive to differences in extension between the vorticity and gradient direction, since it is scaled by the radius of gyration, whose value almost doubles from low to high Weissenberg number.

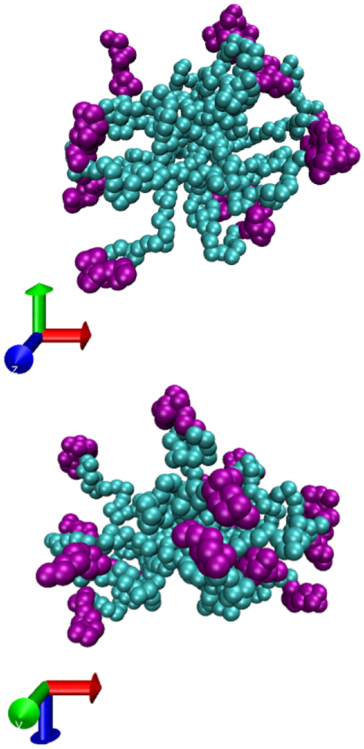

(a) Wi ≈ 0.5

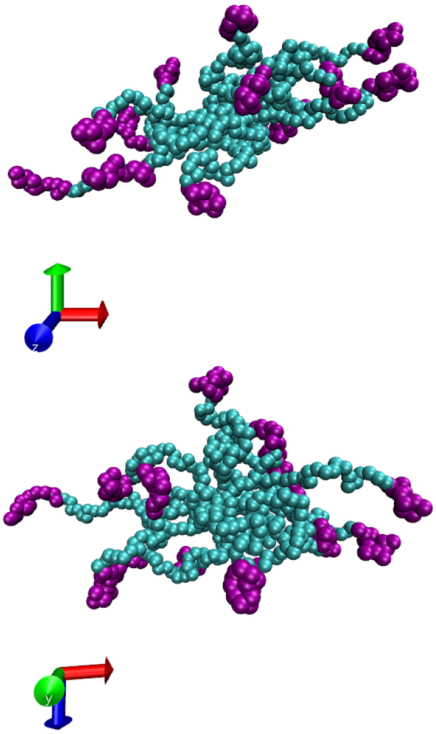

(b) Wi ≈ 30

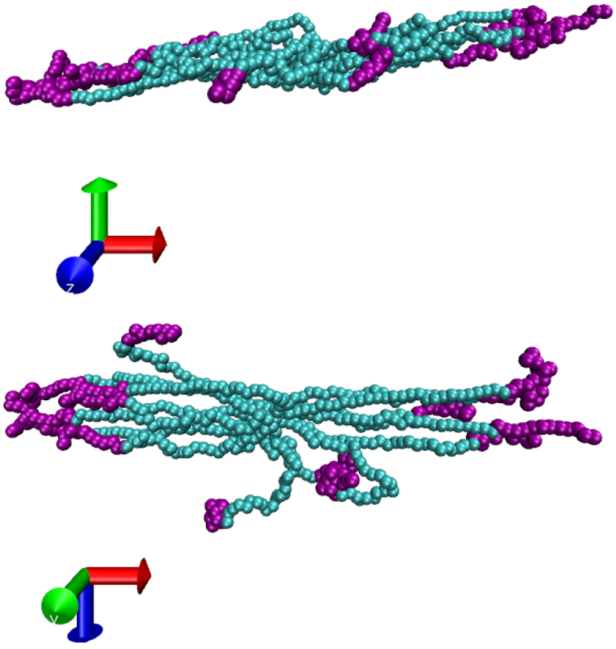

(c) Wi ≈ 560

Figure 5.7: Representative conformations of a TSP with $f = 15$ and $\lambda = 1.05$ at different shear rates. Each conformation is shown in the flow-gradient plane (top) and the flow-vorticity plane (bottom). Purple spheres correspond to solvophobic B-type monomers, while solvophilic A-type monomers are coloured in blue.

5.2.3 Orientational Resistance

As discussed in section 2.2.3 and appendix B, the orientational resistance is a measure for the alignment of a molecule in a flow field. Our results for the orientational resistance as a function of Weissenberg number are presented in figure 5.8 for stars of functionalities 6, 9 and 15, respectively.

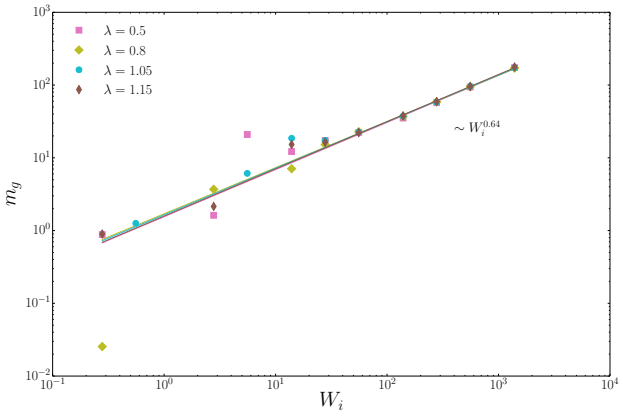

(a) $f = 6$

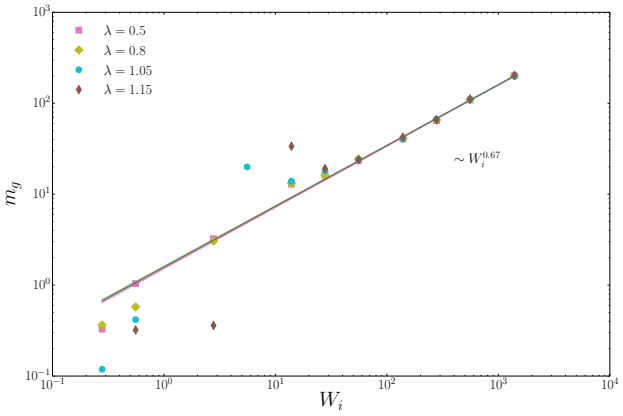

(b) $f = 9$

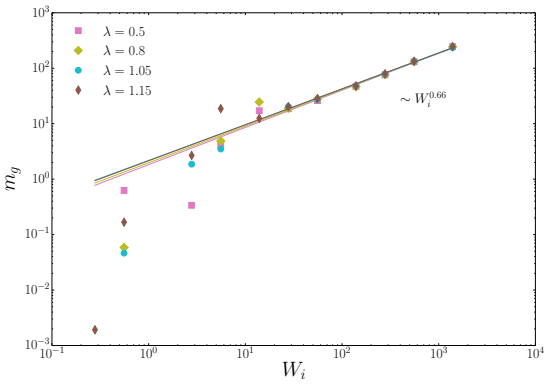

(c) $f = 15$

Figure 5.8: Orientational resistance m_g as a function of Weissenberg number Wi for star polymers of functionalities $f \in \{6, 9, 15\}$ (from left to right and top to bottom) and amphiphilicity $\alpha = 0.3$

Unlike for linear polymer chains, we do not see a plateau value at small shear rates. However, we do observe that the orientational resistance can be described by a powerlaw,

$$m_g(\mathrm{Wi}) \sim \mathrm{Wi}^{\mu}\,, \tag{5.3}$$

for large Weissenberg numbers. A linear fit of the logarithms of both m_g and Wi at the five highest shear rates considered yields the exponents μ as indicated in figures 5.8(a)-(c). These results coincide within the statistical error with the results obtained for purely repulsive star polymers [74], where an exponent of $\mu = 0.65 \pm 0.05$ was found. Furthermore, we see no significant difference in orientational resistance with respect to the inverse temperature λ, which is probably related to the fact that the stretching of the stars in the flow direction at high Weissenberg numbers dominates their shape.

5.3 The Case of High Amphiphilicity $\alpha = 0.5$

We now turn our attention to star-polymers with a higher amphiphilicity, namely $\alpha = 0.5$. For this fraction of attractive monomers, we have found that the number of patches formed by stars of 9 or 15 arms reaches its maximum value at $\lambda = 1.15$ (*cf.* section 2.2.1), which is the highest value of λ considered in our non-equilibrium simulations. Upon further increase of the attraction between the solvophobic tails, different patches collapse onto each other, leading to an on average decreasing number of patches of larger size. We would like to see whether the exertion of shear forces induces a similar behaviour as the modulation of the attractive coupling. We will consider the same star architectures in terms of functionality and attraction and the same Weissenberg numbers as for the case of low amphiphilicity stars (*cf.* section 5.2)

5.3.1 Characterisation of Patchiness

For low values of λ we observe the same monotonic trend of increasing number of patches with increasing shear rate (see left column of figure 5.9), as was already seen in the case of low amphiphilicty. Although small, this trend is now also visible and more conclusive for the patch size, as can be seen from the right column of figure 5.9. For the highest value of λ considered, i.e. $\lambda = 1.15$, however, patch-number and patch-size exhibit an interesting non-monotonicity which differs also for the various functionalities investigated. For these cases, the patch-size is peaked at some low (for $f = 9$) or intermediate (for $f = 6, 15$) Weissenberg number. This behaviour is especially pronounced for the star-architecture with 15 arms, where as little as three to as many as five arms can on average be part of a patch, depending on the shear rate.

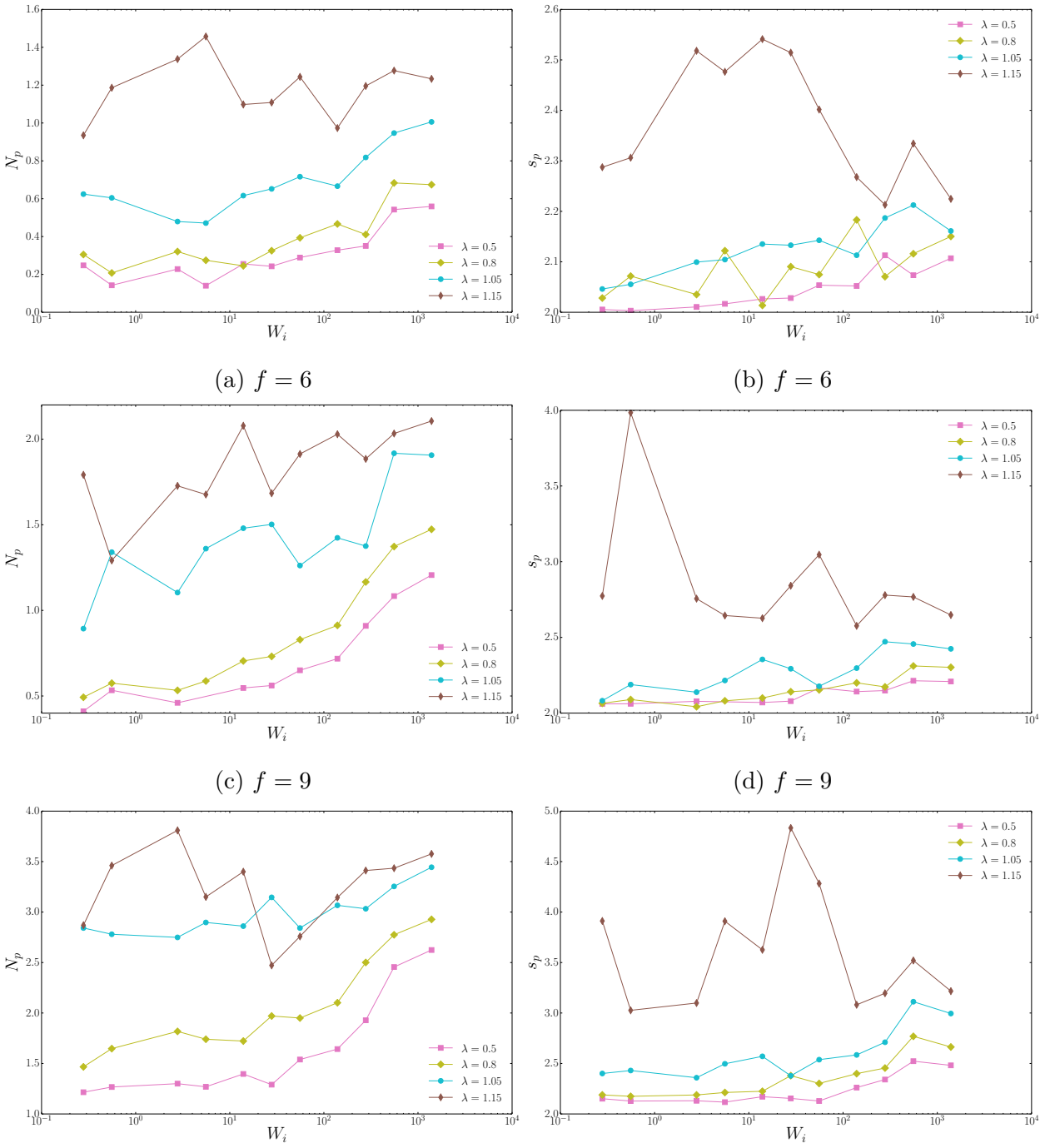

(a) $f = 6$ (b) $f = 6$

(c) $f = 9$ (d) $f = 9$

(e) $f = 15$ (f) $f = 15$

Figure 5.9: Number of patches N_p (left) and patch-size s_p (right) as a function of Weissenberg number Wi for functionalities $f \in \{6, 9, 15\}$ (from top to bottom) and amphiphilicity $\alpha = 0.5$

Since these peeks in patch size go hand in hand with local minima in patch-number, we were interested in whether the average number of arms being part of any patch, i.e. $N_a = N_p \cdot s_p$, remains more or less constant over the range of Weissenberg numbers considered. As can be seen from figure 5.10, this is indeed the case for stars with 9 and 15 arms, apart

from minor fluctuations at intermediate shear rates. This indicates that in these cases shear does not induce the formation of more patches of the same type as present in equilibrium, but rather leads to the reconfiguration of patches. This is an interesting finding, since the number of patches formed by a TSP determines the macroscopic properties at finite densities [11, 12, 15, 14]. These could thus be tuned not only by temperature but also by applying shear to the system. For stars of functionality $f = 6$, the trend in N_a follows that of the number of patches N_p closely, since the patch size varies only between about $s_p = 2.2$ and $s_p = 2.6$.

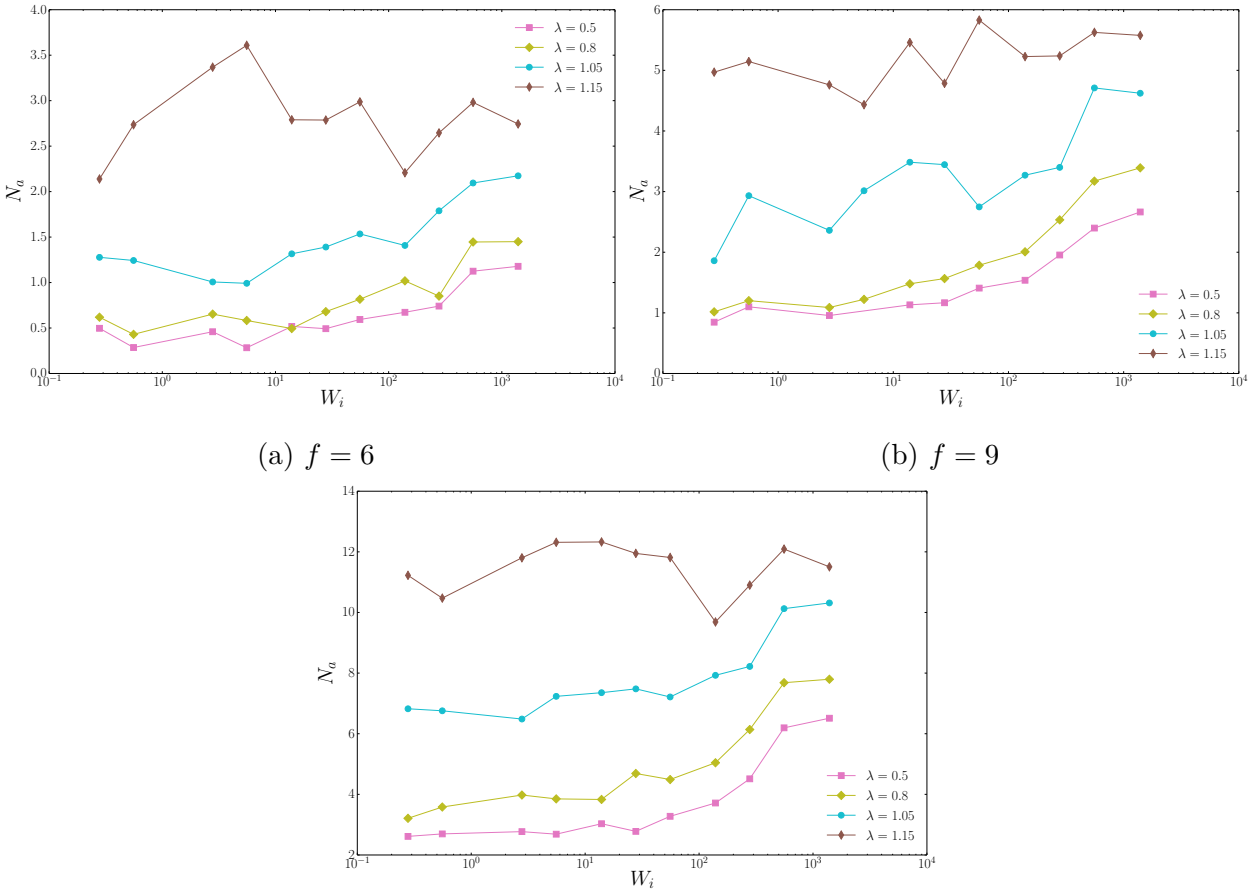

(a) $f = 6$ (b) $f = 9$

(c) $f = 15$

Figure 5.10: Number of arms participating in patch formation N_a as a function of Weissenberg number Wi for functionalities $f \in \{6, 9, 15\}$ (from left to right and top to bottom) and amphiphilicity $\alpha = 0.5$

5.3.2 Conformation and Shape Parameters

At an amphiphilicity of $\alpha = 0.5$, the size of the TSPs, as measured by their average radius of gyration in figure 5.11, is significantly smaller for higher λ throughout the whole range of shear rates considered. This was not the case for low amphiphilicity stars, where the differences completely vanished at high Weissenberg numbers (*cf.* section 5.2.2). Surprisingly, the prolateness S is not affected by the attraction between B-monomers, as depicted in figures 5.12(a), (c) and (e).

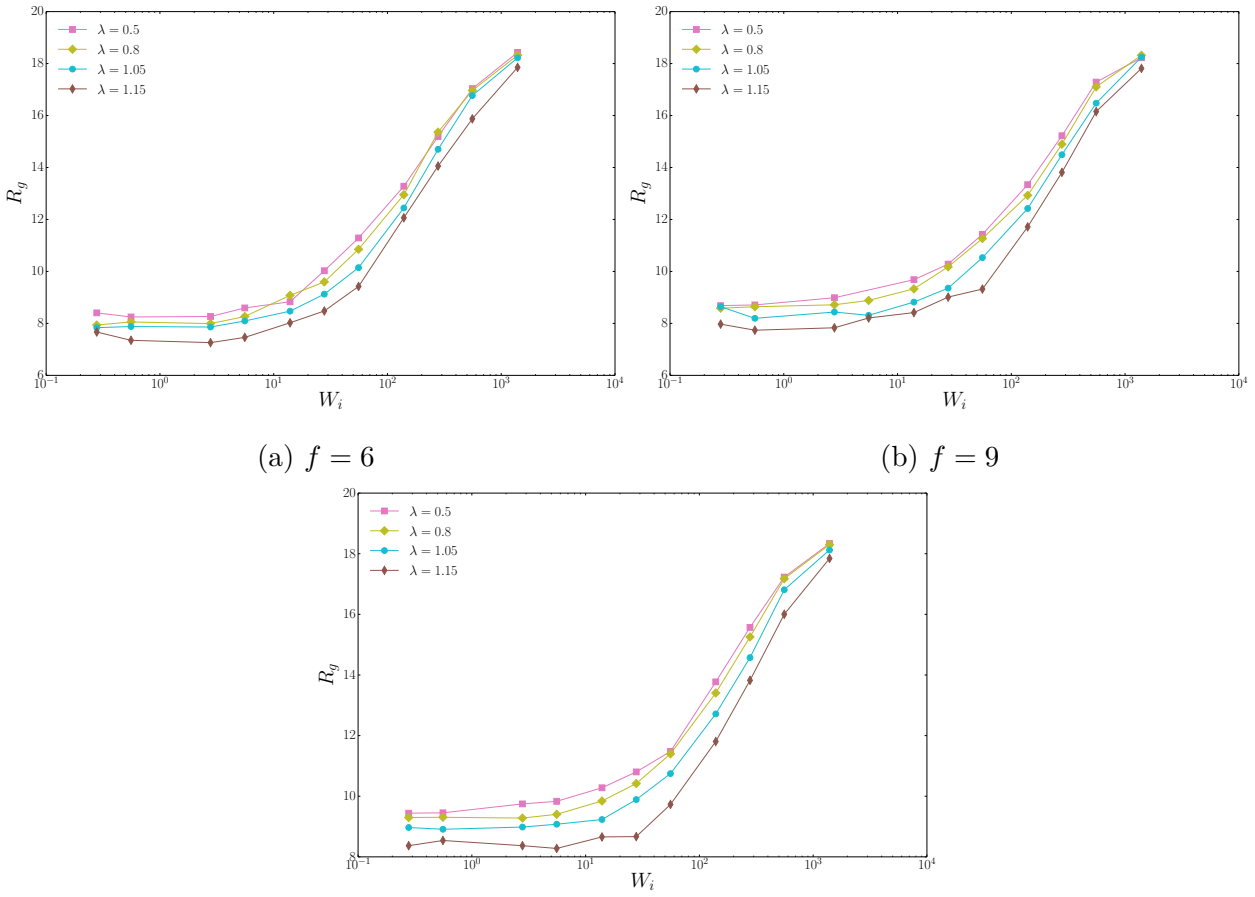

(a) $f = 6$ (b) $f = 9$

(c) $f = 15$

Figure 5.11: Radius of gyration R_g as a function of Weissenberg number Wi for functionalities $f \in \{6, 9, 15\}$ (from left to right and top to bottom) and amphiphilicity $\alpha = 0.5$

For TSPs of low functionality and low attraction between solvophobic monomers, the acylindricity follows the same qualitative trend that has been found for low amphiphilicity stars (*cf.* figures 5.6 and 5.12). For these parameters, the average number of patches does not exceed two at any Weissenberg number and since two patches do not hinder the alignment with the flow field nor break cylindrical symmetry, the acylidricity is completely determined by the strength of the shear flow. A deviation from this behaviour can already be seen

for $f = 9$ and $\lambda = 1.15$, but for stars with 15 arms, the curves for different λ are clearly distinct from each other. We assume that the acylindricity is strongly affected by the number of patches a star forms, since some patch-numbers are more compatible with cylindrical symmetry than others.

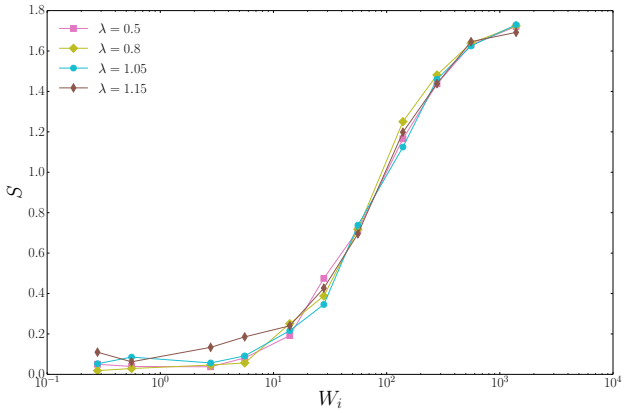

(a) $f = 6$

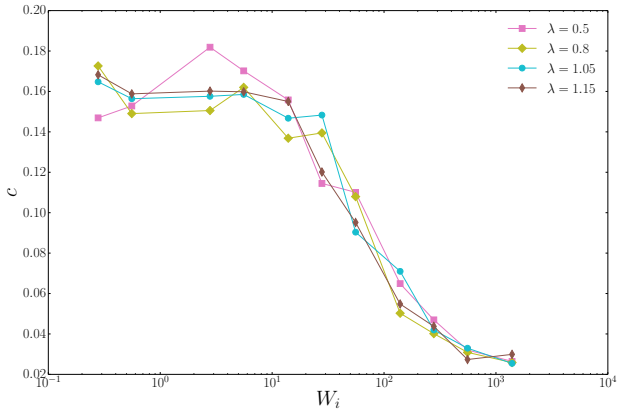

(b) $f = 6$

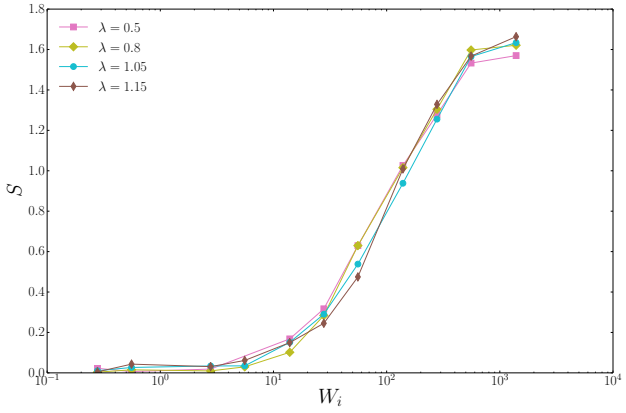

(c) $f = 9$

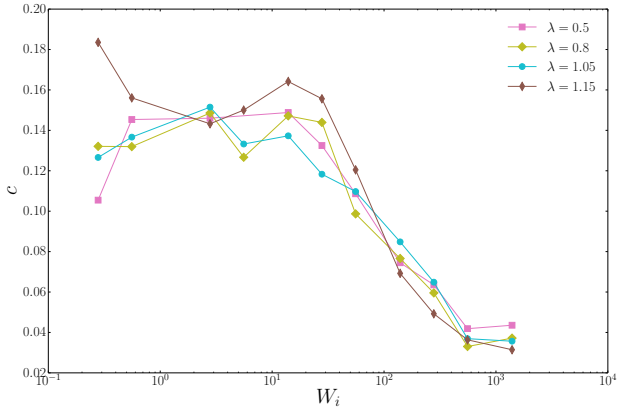

(d) $f = 9$

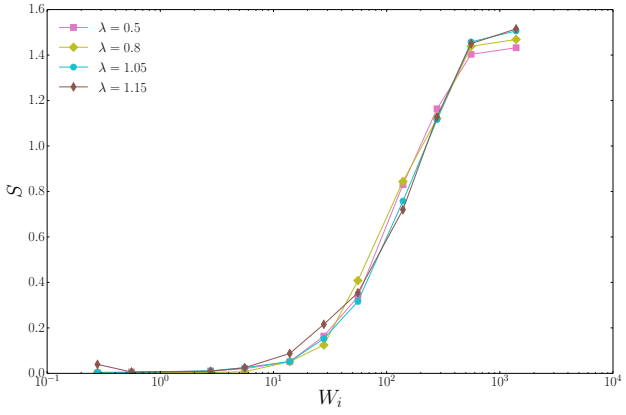

(e) $f = 15$

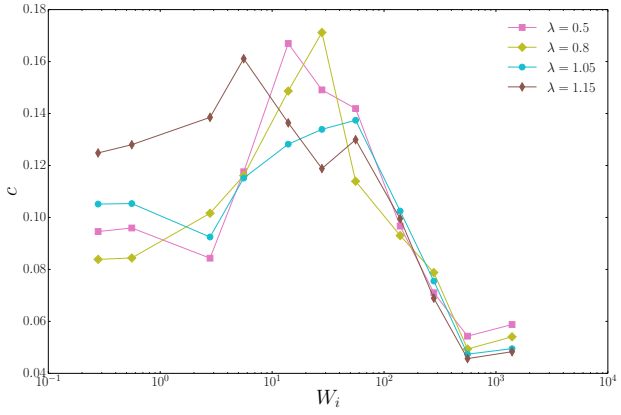

(f) $f = 15$

Figure 5.12: Prolateness S (left) and acylindricity c (right) as a function of Weissenberg number Wi for functionalities $f \in \{6, 9, 15\}$ (from top to bottom) and amphiphilicity $\alpha = 0.5$

Figure 5.13 aims to compare the shape of a star with 15 arms at two different temperatures, corresponding to $\lambda = 0.8$ and $\lambda = 1.15$, and two different shear rates, at which their acylindricity clearly differs. At Wi ≈ 6, the TSP of low λ forms only small patches, while most arms are free, which leads to a highly spherical shape and thus a small acylindricity. The star of $\lambda = 1.15$, however, forms three patches at this Weissenberg number, in which most arms participate. Since this conformation is highly asymmetrical with respect to a rotation around its major axis, it coincides with the maximum in acylindricity. As the shear rate increases further, three patches of approximately equal size are not stable anymore, and one of the patches is broken up and its arms distributed among the remaining ones, which can be easily aligned with the flow. Since the attraction between solvophobic monomers and the formation of two big patches hinders the extension of arms in the vorticity and the gradient direction, the acylindricity is much smaller than for stars of low λ, whose patches are mostly made up of two or three arms.

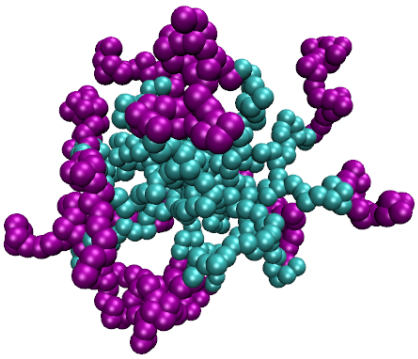

(a) $\lambda = 0.8$, Wi ≈ 6

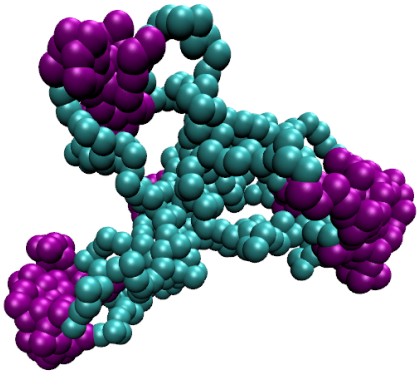

(b) $\lambda = 1.15$, Wi ≈ 6

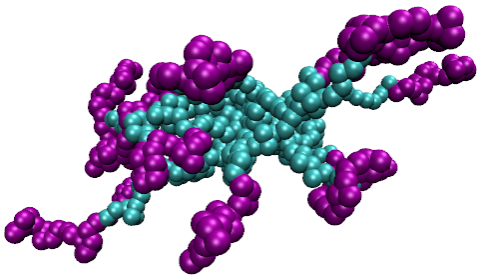

(c) $\lambda = 0.8$, Wi ≈ 140

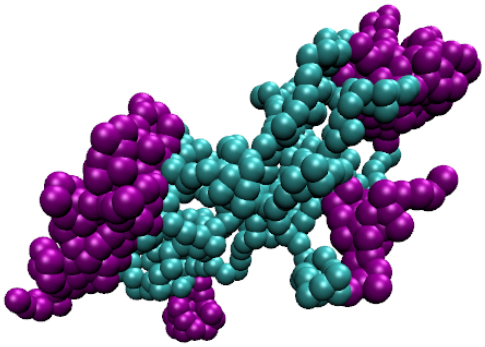

(d) $\lambda = 1.15$, Wi ≈ 1400

Figure 5.13: Representative conformations of TSPs with $f = 15$, $\alpha = 0.5$ and $\lambda = 0.8$ (left) as well as $\lambda = 1.15$ (right) at two different Weissenberg numbers, Wi ≈ 6 (top) and Wi ≈ 30. Purple spheres correspond to solvophobic B-type monomers, while solvophilic A-type monomers are coloured in blue.

5.3.3 Orientational Resistance

The orientational resistance m_g shows marked differences for $\alpha = 0.5$ at high shear rates, depending on the attraction between B-monomers. As depicted in figure 5.14, star-polymers with lower values of λ tend to align themselves more easily with the flow field. On the other hand, the exponents of the fitted curve $m_g \sim \mathrm{Wi}^{\mu}$ are smaller for stars with stronger attraction, since the differences in orientational resistance vanish at very high Weissenberg numbers. Table 5.1 summarizes the findings of the fitting procedure. Again, only the last five data points, which lie on a straight line in the double-logarithmic plot were used for the power-law fit. It should be noted that, although the statistical error is rather high compared to the differences in the exponents, the trend is the same for all functionalities considered.

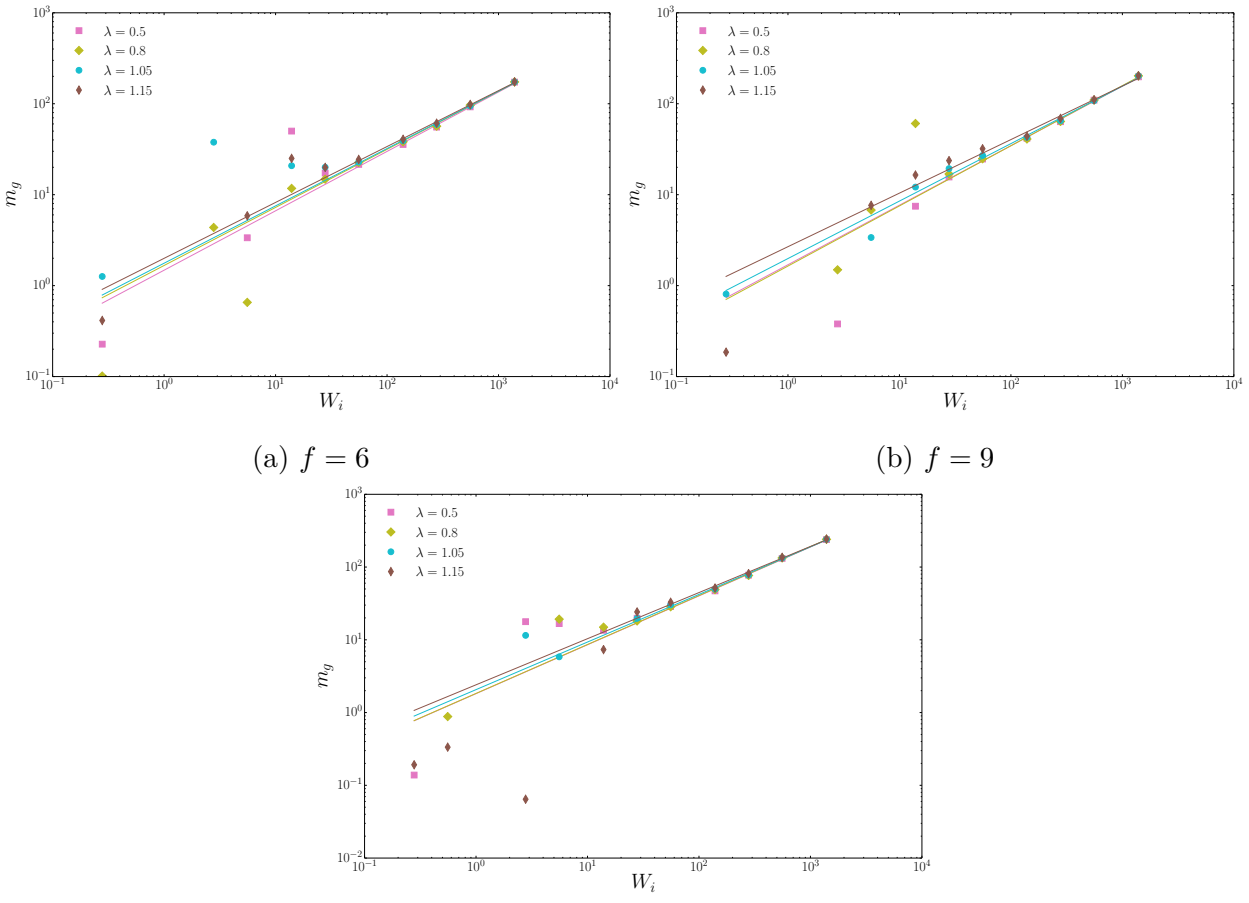

(a) $f = 6$ (b) $f = 9$

(c) $f = 15$

Figure 5.14: Orientational resistance m_g as a function of Weissenberg number Wi for star polymers of functionalities $f \in \{6, 9, 15\}$ (from left to right and top to bottom) and amphiphilicity $\alpha = 0.5$

	μ		
λ	**f = 6**	**f = 9**	**f = 15**
0.5	0.65 ± 0.03	0.66 ± 0.03	0.68 ± 0.03
0.8	0.64 ± 0.03	0.66 ± 0.04	0.67 ± 0.03
1.05	0.63 ± 0.03	0.64 ± 0.03	0.65 ± 0.04
1.15	0.61 ± 0.03	0.59 ± 0.07	0.63 ± 0.04

Table 5.1: Exponents μ of the power law $m_g \sim \mathrm{Wi}^{\mu}$ for amphiphilicity $\alpha = 0.5$ and different inverse temperatures λ and functionalities f.

5.3.4 A closer look at $f = 15$ and $\lambda = 1.15$

Since it exhibits the strongest non-monotonicity and the greatest changes in *patchiness* upon being subjected to different shear rates, we will try to characterise the behaviour of the star architecture with 15 arms and high attraction between solvophobic monomers, i.e. $\lambda = 1.15$ in more detail. To this end, we take a look at typical conformations of this TSP at increasing shear rates as illustrated in figure 5.15. At a Weissenberg number of $\mathrm{Wi} \approx 3$, the shape and patchiness of the star resembles that of the equilibrium simulations, as is also reflected by the fact that all shape parameters are approximately constant up to this shear rate. Increasing the shear rate to intermediate values corresponding to $\mathrm{Wi} \approx 30$, we notice a change from three to four small patches to two or three bigger patches of five arms on average. This transformation in patch configuration is likely due to the elongation of the star (see figure 5.12e) as well as its alignment with the flow field (see 5.14c). Upon further increase of the shear rate (figure 5.15c), we see a strong drop in patch size s_p and the number of patch-forming arms N_a as the shear stresses force the arms to elongate and to break free of the patches. The patches that remain stable are clustered towards the center of the star polymer, leading to a high local density near the anchoring point. At very high shear rates ($\mathrm{Wi} > 10^3$, figure 5.15d), all arms are elongated and new patches can be formed by neighbouring arms aligning with the flow field.

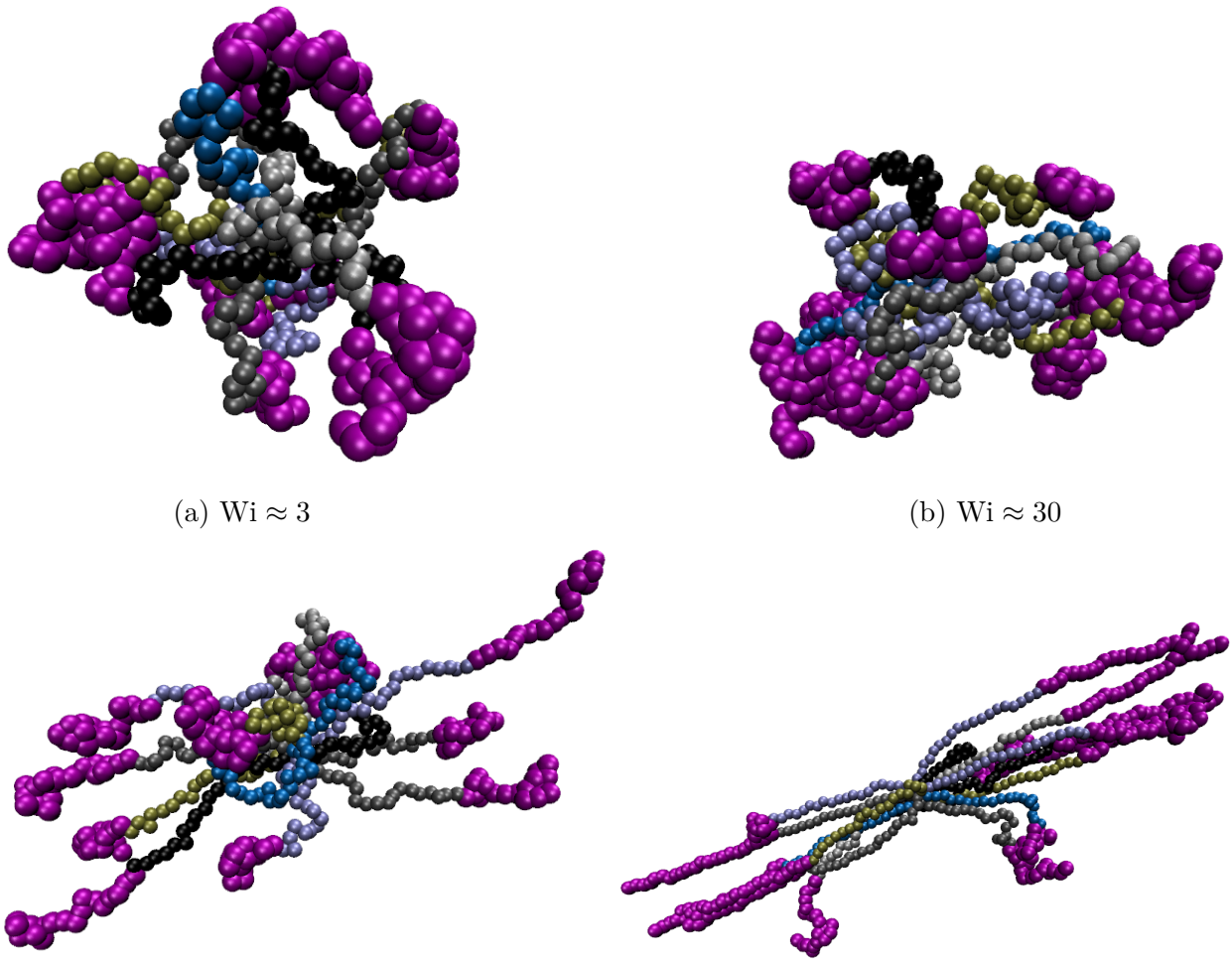

(a) Wi ≈ 3

(b) Wi ≈ 30

(c) Wi ≈ 140

(d) Wi ≈ 1400

Figure 5.15: Representative conformations of a TSP with $f = 15$, $\lambda = 1.15$ and $\alpha = 0.5$ at various Weissenberg numbers (increasing from (a) to (d)). Purple spheres correspond to solvophobic B-type monomers, while solvophilic A-type monomers are coloured in different shades of grey and blue to distuinguish between arms.

Chapter 6

Conclusion and Outlook

In this work, we have performed a first investigation of a specific class of molecules, *telechelic star polymers*, under homogeneous shear flow conditions, employing a simulation technique which couples classic *Molecular Dynamics* to mesoscopic *Multiparticle Collision Dynamics*. The main focus hereby lied on the quantification of the polymers' *patchiness*, their shape parameters and their orientational resistance.

We have shown that these polymers respond to shear stresses qualitatively different from athermal stars, when the attraction between their solvophobic blocks is sufficiently high and that shear can be utilized as yet another parameter to tune their self-assembly next to functionality, amphiphilicity and temperature. While shear increases the *patchiness* of low amphiphility TSPs as a result of their alignment with the flow field, we have found that for high amphiphility stars the number and size of patches formed are non-monotonic functions of shear rate. This might have interesting implications on the system's rheological properties and viscoelastic responses in dilute bulk phases, since the macro- and microscopic phase behaviour of TSPs in equilibrium is governed by their number of association sites, or patches. Furthermore, we were able to demonstrate that high amphiphility TSPs resist alignment with the flow field more strongly than athermal star polymers in the regime of intermediate Weissenberg numbers.

Whether the characteristics of single star polymers found in this study will prevail in systems of finite densities will be subject of further theoretical and computational studies in the future.

Appendix A

Solutions to the Linearized Navier–Stokes Equations

In this appendix, we will derive the solutions to the linearised Navier-Stokes equations and subsequently use these results to determine the velocity autocorrelation functions presented in section 4.7.2 [75, 76].

We will start from the *Navier-Stokes equation* with an added random force term $\boldsymbol{f}^R = \boldsymbol{\nabla} \cdot \boldsymbol{\sigma}^R$ describing thermal fluctuations

$$\rho \left(\frac{\partial \boldsymbol{v}}{\partial t} + (\boldsymbol{v} \cdot \boldsymbol{\nabla}) \boldsymbol{v} \right) = -\nabla p + \eta \Delta \boldsymbol{v} + (\zeta + \frac{1}{3}\eta) \boldsymbol{\nabla} (\boldsymbol{\nabla} \cdot \boldsymbol{v}) + \boldsymbol{f}^R \,, \tag{A.1}$$

together with the continuity equation

$$\frac{\partial \rho}{\partial t} + \nabla \cdot (\rho \boldsymbol{v}) = 0 \,. \tag{A.2}$$

In contrast to section 3.4, where we used the dimensionless *Reynolds number* (*cf.* eq. 3.23) to linearise the *Navier-Stokes equation*, we will now make a linear in expansion in $\boldsymbol{v}$ and ρ. We assume that the density ρ is nearly constant across the fluid with only small variations $\delta\rho$ and that the velocity of the fluid is zero apart from small fluctuations $\delta\boldsymbol{v}$, i.e.

$$\rho = \rho_0 + \delta\rho \qquad \boldsymbol{v} = \delta\boldsymbol{v} \,. \tag{A.3}$$

Substituting A.3 into the *Navier-Stokes equation* A.1 and neglecting terms quadratic in $(\delta\boldsymbol{v}, \delta\rho)$ leads to the linearised equations

$$\rho_0 \frac{\partial \boldsymbol{v}}{\partial t} = -\nabla p + \eta \Delta \boldsymbol{v} + (\zeta + \frac{1}{3}\eta) \boldsymbol{\nabla} (\boldsymbol{\nabla} \cdot \boldsymbol{v}) + \boldsymbol{f}^R \,, \tag{A.4}$$

$$\frac{\partial}{\partial t} \delta\rho + \rho_0 \boldsymbol{\nabla} \cdot \boldsymbol{v} = 0 \,, \tag{A.5}$$

where we wrote $\delta\boldsymbol{v}$ as $\boldsymbol{v}$ for simplicity, but keep in mind that the stationary velocity is still zero. Taking the divergence of of equation A.4 and using equation A.5 to substitute the term $\frac{\partial}{\partial t}\left(\rho_0 \boldsymbol{\nabla}\cdot\boldsymbol{v}\right)$ yields

$$-\frac{\partial^2}{\partial t^2}\delta\rho = -\Delta p + \boldsymbol{\nabla}\cdot\left[\eta\Delta\boldsymbol{v} + (\zeta+\frac{1}{3}\eta)\boldsymbol{\nabla}(\boldsymbol{\nabla}\cdot\boldsymbol{v}) + \boldsymbol{f}^R\right]. \tag{A.6}$$

If we assume that the fluid obeys the ideal gas equation of state

$$p = \frac{Nk_bT}{V} = \rho c^2\,, \tag{A.7}$$

with $c=\sqrt{k_bT/m}$ being the isothermal velocity of sound, we finally arrive at

$$\Delta p - \frac{1}{c^2}\frac{\partial^2 p}{\partial t^2} = \boldsymbol{\nabla}\cdot\left[\eta\Delta\boldsymbol{v} + (\zeta+\frac{1}{3}\eta)\boldsymbol{\nabla}(\boldsymbol{\nabla}\cdot\boldsymbol{v}) + \boldsymbol{f}^R\right]. \tag{A.8}$$

In order to solve equations A.4 and A.8 for the unknown variables $\boldsymbol{v}$ and p, we perform a Fourier transformation of the form

$$\boldsymbol{v}(\boldsymbol{r},t) = \frac{1}{2\pi}\sum_k \int \hat{\boldsymbol{v}}(\boldsymbol{k},\omega)\, e^{-i\boldsymbol{k}\cdot\boldsymbol{r}}\, e^{i\omega t}\mathrm{d}\omega\,, \tag{A.9}$$

$$\hat{\boldsymbol{v}}(\boldsymbol{k},\omega) = \frac{1}{V}\int \boldsymbol{v}(\boldsymbol{r},t)\, e^{i\boldsymbol{k}\cdot\boldsymbol{r}}\, e^{-i\omega t}\mathrm{d}^3r\mathrm{d}t \tag{A.10}$$

on all non-constant variables, which yields

$$i\omega\rho_0\hat{\boldsymbol{v}} = i\boldsymbol{k}\hat{p} - \eta k^2\hat{\boldsymbol{v}} - (\zeta+\frac{1}{3}\eta)\boldsymbol{k}\boldsymbol{k}^T\hat{\boldsymbol{v}} + \hat{\boldsymbol{f}^R}\,, \tag{A.11}$$

$$\left(\frac{\omega^2}{c^2}-k^2\right)\hat{p} = i\boldsymbol{k}^T\left[\eta k^2\hat{\boldsymbol{v}} + (\zeta+\frac{1}{3}\eta)\boldsymbol{k}\boldsymbol{k}^T\hat{\boldsymbol{v}} - \hat{\boldsymbol{f}}^R\right], \tag{A.12}$$

where the superscript T denotes the transpose of a vector.

In order to continue, we separate the velocity $\hat{\boldsymbol{v}}$ into a longitudinal and transverse part with respect to $\boldsymbol{k}$, i.e. $\hat{\boldsymbol{v}} = \hat{\boldsymbol{v}}_L + \hat{\boldsymbol{v}}_T$, and define the longitudinal and transverse projection operators $\boldsymbol{P}_L \coloneqq \boldsymbol{k}\boldsymbol{k}^T/k^2$ and $\boldsymbol{P}_T \coloneqq \mathbb{1} - \boldsymbol{P}_L$, respectively. Applying $\boldsymbol{P}_T$ on equation A.11 yields

$$\hat{\boldsymbol{v}}_T = (i\omega\rho_0)^{-1}\,\boldsymbol{P}_T\boldsymbol{f}^R =: \hat{Q}_T(\boldsymbol{k},\omega)\boldsymbol{P}_T\hat{\boldsymbol{f}}^R\,. \tag{A.13}$$

Multiplying equation A.11 by $\boldsymbol{k}^T$, we can solve for $\hat{p}$

$$\hat{p} = \left(\frac{\omega\rho_0}{k^2} - i\tilde{\eta}\right)\boldsymbol{k}^T\hat{\boldsymbol{v}} + \frac{i}{k^2}\boldsymbol{k}^T\hat{\boldsymbol{f}^R}\,, \tag{A.14}$$

with $\tilde{\eta} = \frac{4\eta}{3}+\zeta$. Substituting into equation A.12, we finally arrive at

$$\hat{\boldsymbol{v}}_L = \left(\eta\tilde{k}^2 + \frac{i\rho_0}{\omega}\right)^{-1}\boldsymbol{P}_L\hat{\boldsymbol{f}^R} =: \hat{Q}_L(\boldsymbol{k},\omega)\boldsymbol{P}_L\hat{\boldsymbol{f}}^R\,. \tag{A.15}$$

In order to calculate the velocity autocorrelation functions, we need to specify some characteristics of the random force $\boldsymbol{f}^R = \boldsymbol{\nabla}\cdot\boldsymbol{\sigma}^R$. Since the random force accounts for thermal fluctuations of the fluid, we assume that the stochastic process for the random stress tensor $\boldsymbol{\sigma}^R$ is Gaussian and Markovian with the following moments

$$\langle \boldsymbol{\sigma}^R \rangle = 0\,, \tag{A.16}$$

$$\langle \boldsymbol{\sigma}^R_{\alpha\beta}(\boldsymbol{r},t)\boldsymbol{\sigma}^R_{\alpha'\beta'}(\boldsymbol{r}'t') = 2k_BT\eta_{\alpha\beta\alpha'\beta'}\delta^3(\boldsymbol{r}-\boldsymbol{r}')\delta(t-t')\,, \tag{A.17}$$

with

$$\eta_{\alpha\beta\alpha'\beta'} = \eta\left(\delta_{\alpha\beta'}\delta_{\alpha'\beta}+\delta_{\alpha\alpha'}\delta_{\beta\beta'}\right)+\left(\zeta-\frac{2}{3}\eta\right)\delta_{\alpha\beta}\delta_{\alpha'\beta'}\,. \tag{A.18}$$

With this, we can calculate the correlation function of the random force in Fourier space

$$\begin{aligned}\langle \hat{f}^R_\alpha(\boldsymbol{k},\omega)\hat{f}^R_\beta(\boldsymbol{k}',\omega')\rangle &= -k_{\alpha'}k_{\beta'}\langle\sigma_{\alpha\alpha'}(\boldsymbol{k},\omega)\sigma_{\beta\beta'}(\boldsymbol{k}',\omega')\rangle \\ &= \frac{4\pi k_BT}{V}k^2\left[\eta\delta_{\alpha\beta}+(\zeta+\frac{\eta}{3})\frac{k_\alpha k_\beta}{k^2}\right]\delta(\omega+\omega')\delta_{\boldsymbol{k},-\boldsymbol{k}}\,,\end{aligned} \tag{A.19}$$

and use this result to find an expression for the velocity autocorrelation function in Fourier space

$$\langle\hat{\boldsymbol{v}}(\boldsymbol{k},\omega)\cdot\hat{\boldsymbol{v}}(\boldsymbol{k}',\omega')\rangle = \frac{4\pi k_BT}{V}k^2\left(2\eta|\hat{Q}_T|^2+\tilde{\eta}|\hat{Q}_L|^2\delta(\omega+\omega')\right)\delta_{\boldsymbol{k},-\boldsymbol{k}}\,. \tag{A.20}$$

Note that the factor 2 in front of $|\hat{Q}_T|^2$ arises from the two transverse components of vorticity.

We will continue now with the derivation of the time-dependent correlation, which follows by convolution

$$\langle\boldsymbol{v}(\boldsymbol{k},t)\cdot\boldsymbol{v}(\boldsymbol{k}',0)\rangle = \frac{2k_BTk^2}{V}\delta_{\boldsymbol{k},-\boldsymbol{k}'}\int\left[2\eta Q_T(\boldsymbol{k},t-t')Q_T(\boldsymbol{k}',-t')+\tilde{\eta}Q_L(\boldsymbol{k},t-t')Q_L(\boldsymbol{k}',-t')\right]\mathrm{d}t'\,. \tag{A.21}$$

Fourier transformation of $Q(\boldsymbol{k},\omega)$ with respect to ω yields

$$Q_T(\boldsymbol{k},t) = \frac{1}{\rho_0}e^{-\nu k^2t}\Theta(t)\,, \tag{A.22}$$

$$Q_L(\boldsymbol{k},t) = \begin{cases}\frac{1}{\rho_0}e^{-\tilde{\nu}k^2t/2}\left[\cos(\Omega t)-\sqrt{\frac{k^2\tilde{\nu}^2}{4c^2-k^2\tilde{\nu}^2}}\sin(\Omega t)\right]\Theta\,, & \text{if } \frac{4c^2}{k^2\tilde{\nu}^2}>1\,,\\ \frac{1}{\rho_0}e^{-\tilde{\nu}k^2t/2}\left[\cosh(\Lambda t)-\sqrt{\frac{k^2\tilde{\nu}^2}{k^2\tilde{\nu}^2-4c^2}}\sinh(\Lambda t)\right]\Theta\,, & \text{if } \frac{4c^2}{k^2\tilde{\nu}^2}<1\,,\end{cases} \tag{A.23}$$

where $\nu=\eta/\rho_0$, $\tilde{\nu}=\tilde{\eta}/\rho_0$, $\Omega = k^2\tilde{\nu}\sqrt{4c^2/(k^2/\tilde{\nu}^2)-1}/2$ and $\Lambda = k^2\tilde{\nu}\sqrt{1-4c^2/(k^2/\tilde{\nu}^2)}/2$. It now remains to evaluate the integral in equation A.21 and separating again into a transverse and longitudinal part to arrive at

$$\langle\boldsymbol{v}^T(\boldsymbol{k},t)\cdot\boldsymbol{v}^T(-\boldsymbol{k},0)\rangle = \frac{2k_BT}{\rho_0V}e^{-\nu k^2|t|}\,, \tag{A.24}$$

$$\langle\boldsymbol{v}^L(\boldsymbol{k},t)\cdot\boldsymbol{v}^L(-\boldsymbol{k},0)\rangle = \begin{cases}\frac{k_BT}{\rho_0V}e^{-\tilde{\nu}k^2|t|/2}\left[\cos(\Omega|t|)-\sqrt{\frac{k^2\tilde{\nu}^2}{4c^2-k^2\tilde{\nu}^2}}\sin(\Omega|t|)\right]\,, & \text{if } \frac{4c^2}{k^2\tilde{\nu}^2}>1\,,\\ \frac{k_BT}{\rho_0V}e^{-\tilde{\nu}k^2|t|/2}\left[\cosh(\Lambda|t|)-\sqrt{\frac{k^2\tilde{\nu}^2}{k^2\tilde{\nu}^2-4c^2}}\sinh(\Lambda|t|)\right]\,, & \text{if } \frac{4c^2}{k^2\tilde{\nu}^2}<1\,.\end{cases} \tag{A.25}$$

Appendix B

On the Derivation of Orientational Resistance Under Shear

Consider a molecule made up of N monomers considered as point particles of equal mass. Its gyration tensor is defined as

$$G_{\alpha\beta} \coloneqq \frac{1}{N}\sum_{i=1}^{N}\langle r_i^\alpha r_i^\beta\rangle \qquad \alpha,\beta \in \{x,y,z\}\,, \tag{B.1}$$

where r_i^α is the α-th Cartesian component of the position $\boldsymbol{r_i}$ of the i-th monomer in the center-of-mass reference frame of the molecule. The eigenvectors of the gyration tensor G define the "moment of inertia ellipsoid" of the molecule. If the molecule is subjected to homogenous shear flow with x being the flow direction, y the gradient direction and z the vorticity direction, i.e. the fluid motion obeys

$$v_x = \dot{\gamma} y\,, \tag{B.2}$$

where $\dot{\gamma}$ is the shear rate, its gyration tensor will change compared to an equilibrium situation. In the vorticity direction z, the system is symmetrical with respect to reflection across the origin, i.e. $z \to -z$, from which it follows that terms $r_i^x r_i^z$ or $r_i^y r_i^z$ are equally likely to occur in the gyration tensor as their negative counterparts $-r_i^x r_i^z$ and $-r_i^y r_i^z$. Thus, the entries G_{xz} and G_{yz} of the gyration tensor will vanish in the ensemble average and the gyration tensor takes on the form

$$G = \begin{pmatrix} G_{xx} & G_{xy} & 0 \\ G_{yx} & G_{yy} & 0 \\ 0 & 0 & G_{zz} \end{pmatrix} \tag{B.3}$$

Furthermore, one of the eigenvectors of the gyration tensor G will point along the vorticity direction z, while the other two will be rotated on the $x-y$ plane (see figure B.1). The

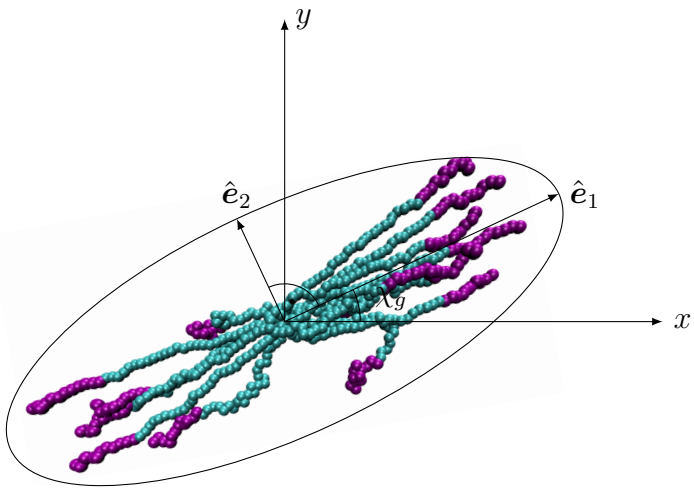

Figure B.1: 2-dimensional projection of the "moment of inertia ellipsoid" defined by the eigenvectors $\hat{\boldsymbol{e}}_1$, $\hat{\boldsymbol{e}}_2$ and $\hat{\boldsymbol{e}}_3$ of the gyration tensor. The eigenvector $\hat{\boldsymbol{e}}_3$ points out of the page. The orientation angle is denoted by χ_g.

angle χ_g denotes the angle between the eigenvector $\hat{\boldsymbol{e}}_1$ and the flow direction x and must lie in the interval $[0, \pi/4]$. Due to the shear forces, $\hat{\boldsymbol{e}}_1$ must correspond to the largest eigenvalue of the gyration tensor, which we will denote by λ_1. Let us consider its defining equation

$$\begin{pmatrix} G_{xx} & G_{xy} & 0 \\ G_{yx} & G_{yy} & 0 \\ 0 & 0 & G_{zz} \end{pmatrix} \begin{pmatrix} e_1^x \\ e_1^y \\ 0 \end{pmatrix} = \lambda_1 \begin{pmatrix} e_1^x \\ e_1^y \\ 0 \end{pmatrix} \tag{B.4}$$

$$\Longrightarrow \begin{cases} G_{xx} e_1^x + G_{xy} e_1^y = \lambda_1 e_1^x \\ G_{yx} e_1^x + G_{yy} e_1^y = \lambda_1 e_1^y \end{cases} \tag{B.5}$$

Since both components, e_x and e_y are positive, it follows that

$$\tan \chi_g = \frac{e_1^y}{e_1^x} \,. \tag{B.6}$$

Dividing both equations in (B.5) allows us to calculate the ratio

$$\frac{e_1^y}{e_1^x} = \frac{G_{yx} e_1^x + G_{yy} e_1^y}{G_{xx} e_1^x + G_{xy} e_1^y} \,, \tag{B.7}$$

$$\begin{aligned} \Longrightarrow \quad & \tan \chi_g = \frac{G_{yx} + G_{yy} \tan \chi_g}{G_{xx} + G_{xy} \tan \chi_g} \,, \\ \Longrightarrow \quad & G_{xx} \tan \chi_g + G_{xy} \tan^2 \chi_g = G_{yx} + G_{yy} \tan \chi_g \,, \\ \Longrightarrow \quad & 1 - \tan^2 \chi_g = \frac{(G_{xx} - G_{yy})}{G_{xy}} \tan \chi_g \,, \end{aligned} \tag{B.8}$$

Using the trigonometric identity

$$\tan 2\alpha = \frac{2\tan\alpha}{1-\tan^2\alpha}\,, \tag{B.9}$$

we finally find that

$$\tan 2\chi_g = \frac{2G_{xy}}{(G_{xx}-G_{yy})}\,. \tag{B.10}$$

Since the tangens is a strictly monotonically increasing function in the interval $(-\frac{\pi}{2}, \frac{\pi}{2})$, it is a good choice for measuring the resistance of a molecule to be oriented in the presence of shear flow and thus the orientational resistance parameter m_G is defined as

$$m_g = \mathrm{Wi}\tan 2\chi_g\,, \tag{B.11}$$

where Wi is the Weissenberg number (*cf.* equation 2.15).

Appendix C

Abstract (english)

Telechelic star polymers (TSPs), consisting of f amphiphilic diblock-copolymer arms anchored to a central point, represent a class of highly tunable nanoparticles with the ability of spontaneously self-assembling into soft patchy particles with attractive aggregation sites formed by the solvophobic parts on their periphery. In this thesis, the patchiness, shape and orientational resistance of said polymers is examined under homogeneous shear flows. This is achieved by employing a hybrid algorithm combining Molecular Dynamics for the monomers with the mesoscopic technique of Multiparticle Collision Dynamics for the solvent. Telechelic star polymers of functionalities $f = \{6, 9, 15\}$ with a fraction of solvophobic monomers of $\alpha = 0.3$ and $\alpha = 0.5$ are considered. The coupling constant governing the attraction between solvophobic monomers is varied from $\lambda = 0.5$ to $\lambda = 1.15$. We find that shear flow promotes patch formation for stars exhibiting little clustering of their solvophobic monomers in equilibrium conditions due to the alignment of the arms with the flow field. For telechelic star polymers of high amphiphilicity and attraction between solvophobic monomers, however, we discover a non-monotonic dependence of patch number and patch size on shear rate. We compare the shape and alignment with the flow of TSPs with that of athermal stars and observe a stronger resistance against alignment at intermediate shear rates. Finally, we propose explanations for the dynamic reorganisation of the solvophobic patches when subjected to shear stresses and make assumptions about their implications on rheological properties in dilute systems.

Appendix D

Abstract (deutsch)

Telechelische Sternpolymere (TSPs), bestehend aus f amphiphilen Diblock-Kopolymeren verankert an einem zentralen Punkt, stellen eine Klasse von leicht manipulierbaren Nanopartikeln mit der Fähigkeit zur spontanen Selbstorganisation zu weichen Kolloiden mit attraktiven Aggregationszentren an ihrer Peripherie dar. In dieser Arbeit wurde die Anzahl und Größe besagter Aggregationszentren, die Form, sowie die Resistenz gegen Orientierung in einer Strömung unter homogener Scherung untersucht. Hierfür wurde ein hybrider Algorithmus verwendet, welcher aus einer Kombination von Molekulardynamik zur Simulation der Monomere und der mesoskopischen Technik "Multiparticle Collision Dynamics" zur Simulation der Fluidteilchen bestand. Es wurden telechelische Sternpolymere der Funktionalitäten $f = \{6, 9, 15\}$, sowie mit einem Anteil an solvophoben Monomeren von $\alpha = 0.3$ und $\alpha = 0.5$ betrachtet. Die Kopplungskonstante λ, welche die Attraktivität zwischen solvophoben Teilchen bestimmt, wurde dabei zwischen $\lambda = 0.5$ und $\lambda = 1.15$ variiert. Es zeigte sich hierbei, dass Scherung Clusterbildung für jene Sternpolymere verstärkt, die in Gleichgewichtssituationen wenig attraktive Aggregationsszentren aufweisen. Dies lässt sich auf deren Ausrichtung im Strömungsprofil der Flüssigkeit zurückführen. Für telechelische Sternpolymere mit hoher Amphiphilizität und Anziehung zwischen deren solvophoben Anteilen konnten wir allerdings eine nicht-monotone Abhängigkeit der Anzahl und Größe der solvophoben Cluster von der Schergeschwindigkeit feststellen. Des weiteren wurden Form und Orientierung der telechelischen Sterne mit jenen von athermalen Sternen verglichen und eine stärkere Resistenz gegen Ausrichtung in der Strömung beobachtet. Zum Schluss wird eine Erklärung für die dynamische Reorganisation der solvophoben Aggregate unter dem Einfluss von Scherspannung angeboten und Annahmen zu deren Implikationen für rheologische Eigenschaften getätigt.

Acknowledgements

First and foremost I would like to thank my supervisor Professor Christos Likos for his invaluable help and advise. I am very grateful for the fact that he always had an open ear for questions and time for scientific discussions.

In addition, I would like to express my gratitude to the whole group of Computational Physics at the University of Vienna, who made me feel very welcome during my stay at their office. In particular, I want to thank Lorenzo Rovigatti for introducing me into the field of telechelic star polymers and navigating me through my first coding attempts for this project, Lisa Weiß for continuous mutual exchange of thoughts on emerging problems and their solutions while working with the *MPC* method, Peter Poier for teaching me about the efficient usage of the Vienna Scientific Cluster, Ronald Blaak for valuable insights into physical reasoning and David Toneian for helpful discussions about good coding practice.

Additionally, I am grateful for having been able to participate in the IHRS BioSoft Guest Student Program at Forschungszentrum Juelich, where I learned a lot about the *MPC* method and had a first look into scientific practice. In this regard, I want to express my thanks to Professor Roland Winkler and Professor Gerhard Gompper for this great opportunity as well as to Mario Theers for his wonderful supervision during my stay.

Last but not least, I would like to address my gratitude toward my loving family and friends. Word cannot express how thankful I am to my mother, Susanne Formanek, and my father, Sepp Linhart, for supporting me throughout my studies, for giving me the time I needed to finish at my own pace and for listening to my explanations about a subject that is so different from theirs. Finally, I wish to give special thanks to my friends Patrick Derflinger and Felicitas Natmessnig for their encouragement in times when I didn't believe I would ever get here.

Bibliography

[1] A. Jusufi and C. N. Likos, "Colloquium: Star-branched polyelectrolytes: The physics of their conformations and interactions," *Rev. Mod. Phys*, vol. 81, no. 4, p. 1753, 2009.

[2] E. Bianchi, J. Largo, P. Tartaglia, E. Zaccarelli, and F. Sciortino, "Phase diagram of patchy colloids: towards empty liquids," *Phys. Rev. Lett.*, vol. 97, no. 16, p. 168301, 2006.

[3] A. B. Pawar and I. Kretzschmar, "Fabrication, assembly, and application of patchy particles," *Macromol. Rapid Comm.*, vol. 31, no. 2, pp. 150–168, 2010.

[4] E. Bianchi, B. Capone, G. Kahl, and C. N. Likos, "Soft-patchy nanoparticles: modeling and self-organization," *Faraday Discuss.*, vol. 181, pp. 123–138, 2015.

[5] D. Nykypanchuk, M. M. Maye, D. van der Lelie, and O. Gang, "Dna-guided crystallization of colloidal nanoparticles," *Nature*, vol. 451, no. 7178, pp. 549–552, 2008.

[6] S. Y. Park, A. K. Lytton-Jean, B. Lee, S. Weigand, G. C. Schatz, and C. A. Mirkin, "Dna-programmable nanoparticle crystallization," *Nature*, vol. 451, no. 7178, pp. 553–556, 2008.

[7] B. M. Mladek, G. Kahl, and C. N. Likos, "Computer assembly of cluster-forming amphiphilic dendrimers," *Phys. Rev. E*, vol. 100, no. 2, p. 028301, 2008.

[8] D. Gottwald, C. N. Likos, G. Kahl, and H. Löwen, "Ionic microgels as model systems for colloids with an ultrasoft electrosteric repulsion: Structure and thermodynamics," *J. Chem. Phys.*, vol. 122, no. 7, p. 074903, 2005.

[9] F. Lo Verso, C. N. Likos, C. Mayer, and H. Löwen, "Collapse of telechelic star polymers to watermelon structures," *Phys. Rev. Lett.*, vol. 96, p. 187802, May 2006.

[10] F. Lo Verso, C. N. Likos, and H. Löwen, "Computer simulation of thermally sensitive telechelic star polymers," *J. Phys. Chem. C*, vol. 111, no. 43, pp. 15803–15810, 2007.

[11] F. Lo Verso, A. Z. Panagiotopoulos, and C. N. Likos, "Aggregation phenomena in telechelic star polymer solutions," *Phys. Rev. E*, vol. 79, p. 010401, Jan 2009.

[12] F. Lo Verso, A. Z. Panagiotopoulos, and C. N. Likos, "Phase behavior of low-functionality, telechelic star block copolymers," *Faraday Discuss.*, vol. 144, pp. 143–157, 2010.

[13] B. Capone, I. Coluzza, F. LoVerso, C. N. Likos, and R. Blaak, "Telechelic star polymers as self-assembling units from the molecular to the macroscopic scale," *Phys. Rev. Lett.*, vol. 109, p. 238301, Dec 2012.

[14] C. Koch, A. Z. Panagiotopoulos, F. L. Verso, and C. N. Likos, "Customizing worm-like mesoscale structures via self-assembly of amphiphilic star polymers," *Soft matter*, vol. 11, no. 18, pp. 3530–3535, 2015.

[15] C. Koch, C. N. Likos, A. Z. Panagiotopoulos, and F. Lo Verso, "Self-assembly scenarios of block copolymer stars," *Mol. Phys.*, vol. 109, no. 23-24, pp. 3049–3060, 2011.

[16] B. Capone, I. Coluzza, R. Blaak, F. Lo Verso, and C. N. Likos, "Hierarchical self-assembly of telechelic star polymers: from soft patchy particles to gels and diamond crystals," *New. J. Phys.*, vol. 15, no. 9, p. 095002, 2013.

[17] H. Yang and S. T. Lopina, "Penicillin v-conjugated peg-pamam star polymers," *J. Biomater. Sci. Polym. Ed.*, vol. 14, no. 10, pp. 1043–1056, 2003.

[18] G. S. Grest, L. J. Fetters, J. S. Huang, and D. Richter, "Star polymers: experiment, theory, and simulation," *AJ. Chem. Phys.*, vol. 94, p. 67, 2009.

[19] M. Ripoll, R. G. Winkler, and G. Gompper, "Hydrodynamic screening of star polymers in shear flow," *Eur. Phys. J. E*, vol. 23, no. 4, pp. 349–354, 2007.

[20] R. E. Teixeira, H. P. Babcock, E. S. Shaqfeh, and S. Chu, "Shear thinning and tumbling dynamics of single polymers in the flow-gradient plane," *Macromolecules*, vol. 38, no. 2, pp. 581–592, 2005.

[21] Y. Navot, "Elastic membranes in viscous shear flow," *Phys. Fluids*, vol. 10, no. 8, pp. 1819–1833, 1998.

[22] L. Rovigatti, B. Capone, and C. N. Likos, "Soft self-assembled nanoparticles with temperature-dependent properties," *Nanoscale*, vol. 8, pp. 3288–3295, 2016.

[23] H. W. Spiess, "Dynamics of polymeric liquids," *Berichte der Bunsengesellschaft für physikalische Chemie*, vol. 91, no. 12, pp. 1397–1398, 1987.

[24] J. E. Jones, "On the determination of molecular fields. ii. from the equation of state of a gas," *P. Roy. Soc. Lond. A*, vol. 106, no. 738, pp. 463–477, 1924.

[25] M. P. Allen and D. J. Tildesley, *Computer simulation of liquids*. Oxford UP, 1989.

[26] G. S. Grest, K. Kremer, and T. A. Witten, "Structure of many arm star polymers: a molecular dynamics simulation," *Macromolecules*, vol. 20, no. 6, pp. 1376–1383, 1987.

[27] K. Šolc and W. Stockmayer, "Statistical mechanics of random-flight chains. iv. size and shape parameters of cyclic, star-like, and comb-like chains," *Macromolecules*, vol. 6, no. 3, pp. 378–385, 1973.

[28] D. N. Theodorou and U. W. Suter, "Shape of unperturbed linear polymers: polypropylene," *Macromolecules*, vol. 18, no. 6, pp. 1206–1214, 1985.

[29] J. Rudnick and G. Gaspari, "The asphericity of random walks," *J. Phys. A*, vol. 19, no. 4, p. L191, 1986.

[30] J. Aronovitz and D. Nelson, "Universal features of polymer shapes," *J. Phys. Paris*, vol. 47, no. 9, pp. 1445–1456, 1986.

[31] G. Zifferer and W. Preusser, "Monte carlo simulation studies of the size and shape of ring polymers," *Macromol. Theor. Simul.*, vol. 10, no. 5, pp. 397–407, 2001.

[32] M. O. Steinhauser, "A molecular dynamics study on universal properties of polymer chains in different solvent qualities. part i. a review of linear chain properties," *J. Chem. Phys.*, vol. 122, no. 9, 2005.

[33] O. Jagodzinski, E. Eisenriegler, and K. Kremer, "Universal shape properties of open and closed polymer chains: renormalization group analysis and monte carlo experiments," *J. Phys. I*, vol. 2, no. 12, pp. 2243–2279, 1992.

[34] G. Doppelbauer, E. G. Noya, E. Bianchi, and G. Kahl, "Self-assembly scenarios of patchy colloidal particles," *Soft Matter*, vol. 8, no. 30, pp. 7768–7772, 2012.

[35] J. Bossart and H. C. Oettinger, "Orientation of polymer coils in dilute solutions undergoing shear flow: Birefringence and light scattering," *Macromolecules*, vol. 28, no. 17, pp. 5852–5860, 1995.

[36] G. S. Grest, K. Kremer, S. T. Milner, and T. A. Witten, "Relaxation of self-entangled many-arm star polymers," *Macromolecules*, vol. 22, no. 4, pp. 1904–1910, 1989.

[37] R. Bird, C. Curtiss, R. Armstrong, and O. Hassager, *Dynamics of Polymer Liquids Vol. 2 Kinetic Theory*. Wiley, 1987.

[38] H. C. Öttinger, "Gaussian approximation for rouse chains with hydrodynamic interaction," *J. Chem. Phys.*, vol. 90, no. 1, pp. 463–473, 1989.

[39] H. C. Öttinger and Y. Rabin, "Renormalization-group calculation of viscometric functions based on conventional polymer kinetic theory," *J. Non-Newton. Fluid*, vol. 33, no. 1, pp. 53 – 93, 1989.

[40] L. Landau and E. Lifshitz, "Fluid mechanics," *Course of Theoretical Physics*, 1959.

[41] G. P. Morriss and D. J. Evans, *Statistical Mechanics of Nonequilbrium Liquids*. Academic Press, 1990.

[42] J. K. Dhont, *An introduction to dynamics of colloids*. Elsevier, 1996.

[43] G. G. Stokes, "On the Effect of the Internal Friction of Fluids on the Motion of Pendulums," *Cambr. Phil. Soc. Trans.*, vol. 9, p. 8, 1851.

[44] O. Reynolds, "An experimental investigation of the circumstances which determine whether the motion of water shall be direct or sinuous, and of the law of resistance in parallel channels.," *P. Roy. Soc. Lond.*, vol. 35, no. 224-226, pp. 84–99, 1883.

[45] E. M. Purcell, "Life at low reynolds number," *Am. J. Phys.*, vol. 45, no. 1, pp. 3–11, 1977.

[46] A. Malevanets and R. Kapral, "Mesoscopic model for solvent dynamics," *J. Chem. Phys.*, vol. 110, no. 17, pp. 8605–8613, 1999.

[47] A. Malevanets and R. Kapral, "Solute molecular dynamics in a mesoscale solvent," *J. Chem. Phys.*, vol. 112, no. 16, pp. 7260–7269, 2000.

[48] A. Malevanets and J. M. Yeomans, "Dynamics of short polymer chains in solution," *Europhys. Lett.*, vol. 52, no. 2, p. 231, 2000.

[49] H. Noguchi and G. Gompper, "Dynamics of fluid vesicles in shear flow: Effect of membrane viscosity and thermal fluctuations," *Phys. Rev. E*, vol. 72, p. 011901, Jul 2005.

[50] B. Kowalik and R. G. Winkler, "Multiparticle collision dynamics simulations of viscoelastic fluids: Shear-thinning gaussian dumbbells," *J. Chem. Phys.*, vol. 138, no. 10, 2013.

[51] U. Frisch, B. Hasslacher, and Y. Pomeau, "Lattice-gas automata for the navier-stokes equation," *Phys. Rev. Lett.*, vol. 56, pp. 1505–1508, Apr 1986.

[52] G. Gompper, T. Ihle, D. M. Kroll, and R. G. Winkler, *Multi-Particle Collision Dynamics: A Particle-Based Mesoscale Simulation Approach to the Hydrodynamics of Complex Fluids*, p. 1. 2009.

[53] T. Ihle and D. M. Kroll, "Stochastic rotation dynamics. i. formalism, galilean invariance, and green-kubo relations," *Phys. Rev. E*, vol. 67, p. 066705, Jun 2003.

[54] T. Ihle and D. Kroll, "Stochastic rotation dynamics: a galilean-invariant mesoscopic model for fluid flow," *Phys. Rev. E*, vol. 63, no. 2, p. 020201, 2001.

[55] T. Ihle, E. Tüzel, and D. M. Kroll, "Equilibrium calculation of transport coefficients for a fluid-particle model," *Phys. Rev. E*, vol. 72, no. 4, p. 046707, 2005.

[56] C. Pooley and J. Yeomans, "Kinetic theory derivation of the transport coefficients of stochastic rotation dynamics," *J. Phys. Chem. B*, vol. 109, no. 14, pp. 6505–6513, 2005. PMID: 16851730.

[57] M. Ripoll, K. Mussawisade, R. G. Winkler, and G. Gompper, "Low-reynolds-number hydrodynamics of complex fluids by multi-particle-collision dynamics," *Europhys. Lett.*, vol. 68, no. 1, p. 106, 2004.

[58] I. O. Götze, H. Noguchi, and G. Gompper, "Relevance of angular momentum conservation in mesoscale hydrodynamics simulations," *Phys. Rev. E*, vol. 76, p. 046705, Oct 2007.

[59] J. F. Ryder, *Mesoscopic simulations of complex fluids*. PhD thesis, U Oxford, 2005.

[60] H. Noguchi, N. Kikuchi, and G. Gompper, "Particle-based mesoscale hydrodynamic techniques," *Europhys. Lett.*, vol. 78, no. 1, p. 10005, 2007.

[61] M. Theers and R. G. Winkler, "Bulk viscosity of multiparticle collision dynamics fluids," *Phys. Rev. E*, vol. 91, p. 033309, Mar 2015.

[62] M. Theers, E. Westphal, G. Gompper, and R. G. Winkler, "From local to hydrodynamic friction in brownian motion: A multiparticle collision dynamics simulation study," *Phys. Rev. E*, vol. 93, p. 032604, Mar 2016.

[63] C. Huang, A. Chatterji, G. Sutmann, G. Gompper, and R. Winkler, "Cell-level canonical sampling by velocity scaling for multiparticle collision dynamics simulations," *J. Comp. Phys.*, vol. 229, no. 1, pp. 168 – 177, 2010.

[64] G. Bussi, D. Donadio, and M. Parrinello, "Canonical sampling through velocity rescaling," *J. Chem. Phys.*, vol. 126, no. 1, p. 014101, 2007.

[65] S. H. Lee and R. Kapral, "Mesoscopic description of solvent effects on polymer dynamics," *J. Chem. Phys.*, vol. 124, no. 21, 2006.

[66] Y. Inoue, Y. Chen, and H. Ohashi, "Development of a simulation model for solid objects suspended in a fluctuating fluid," *J. Stat. Phys.*, vol. 107, no. 1-2, pp. 85–100, 2002.

[67] M. Born and T. von Kármán, "Über schwingungen in raumgittern," *Physikalische Zeitschrift*, vol. 13, no. 297-309, p. 18, 1912.

[68] D. Goldberg, "What every computer scientist should know about floating-point arithmetic," *ACM Comput. Surv.*, vol. 23, no. 1, pp. 5–48, 1991.

[69] A. Lees and S. Edwards, "The computer study of transport processes under extreme conditions," *J. Phys. C*, vol. 5, no. 15, p. 1921, 1972.

[70] M. Ripoll, K. Mussawisade, R. G. Winkler, and G. Gompper, "Dynamic regimes of fluids simulated by multiparticle-collision dynamics," *Phys. Rev. E*, vol. 72, p. 016701, Jul 2005.

[71] L. Verlet, "Computer "experiments" on classical fluids. i. thermodynamical properties of lennard-jones molecules," *Phys. Rev.*, vol. 159, pp. 98–103, Jul 1967.

[72] D. Frenkel and B. Smit, *Understanding molecular simulations: from algorithms to applications*. Academic Press, 1996.

[73] D. J. Auerbach, W. Paul, A. F. Bakker, C. Lutz, W. E. Rudge, and F. F. Abraham, "A special purpose parallel computer for molecular dynamics: motivation, design, implementation, and application," *J. Phys. Chem.*, vol. 91, no. 19, pp. 4881–4890, 1987.

[74] M. Ripoll, R. G. Winkler, and G. Gompper, "Star polymers in shear flow," *Phys. Rev. Lett.*, vol. 96, p. 188302, May 2006.

[75] C.-C. Huang, G. Gompper, and R. G. Winkler, "Hydrodynamic correlations in multiparticle collision dynamics fluids," *Phys. Rev. E*, vol. 86, p. 056711, Nov 2012.

[76] J. Dhont, G. Gompper, G. Meier, D. Richter, G. Vliegenhart, and R. Zorn, eds., *Functional Soft Matter*, vol. 46 of *Lecture Notes on the IFF Spring School*. FZ Jülich, 2015.